1   **Re-channelization of turbidity currents in South China Sea abyssal plain**

2   **due to seamounts and ridges**

3   **Shaoru Yin[1,*], Ed L. Pope[2], Lin Lin[3,*], Weifeng Ding[1], Jinyao Gao[1], Ziyin Wu[1],**

4   **Chunguo Yang[1] , Jiangxin Chen[4,*], Jiabiao Li[1]**

5   [1]Key Laboratory of Submarine Geosciences, Second Institute of Oceanography,

6   Ministry of Natural Resources, Hangzhou 310012, China

7   [2]Department of Geography, Durham University, Science Laboratories, South Road,

8   Durham, DH1 3LE, United Kingdom

9   [3]Guangzhou Marine Geological Survey, Guangzhou 510075, China

10   [4]Key Laboratory of Gas Hydrate, Qingdao Institute of Marine Geology, Qingdao

11   266071, China

12   [*]Corresponding author: Shaoru Yin (shaoru2017@outlook.com), Lin Lin

13   (linlin_gmgs@163.com), Jiangxin Chen (jiangxin_chen@sina.com)

14   **Highlights:**

15   • A downstream abyssal plain transition from deposition to channels is

16   documented

17   • This is a new example of turbidity current re-channelization

18   • The setting is a flat, open plain, upstream of an area of seamounts and ridges

19   • Turbidity currents traversing this terrain transition from depositional to erosive

20   flows

21   • This confinement results in an increase in coarse sediment content in abyssal

22   plain around the seamount area/fossil spreading center.

23

24   **Abstract**

25   Turbidity currents can be characterized as net-erosive, net-depositional or net-

26   bypassing. Whether a flow is erosive, depositional or bypasses depends on the flow

27   velocity, concentration and size but these can also be impacted by external controls

28   such as the degree of confinement, slope gradient and substrate type and erodibility.

29   Our understanding of the relative importance of these controls comes from laboratory

30   experiments and numerical modelling, as well as from field data due to the proliferation

31   of high-resolution 3D seismic and bathymetric data, as well as the outcrop and rock

32   record. In this study, based on extensive multibeam and seismic reflection surveys in

33   combination with International Ocean Discovery Program cores from the South China

34   Sea, we document a new mechanism of turbidity current transformation from

35   depositional to erosive resulting in channel incision. We show how confinement by

36   seamounts and bedrock highs of previously unconfined turbidity currents has resulted

37   in the development of seafloor channels. These channels are inferred to be the result of

38   confinement of flows, which have traversed the abyssal plain, leading to flow

39   acceleration allowing them to erode the seafloor substrate. This interpretation is further

40 supported by the coarsening of flow deposits within the area of the seamounts,

41 indicating that confinement has increased flow competency, allowing turbidity currents

42 to carry larger volumes of coarse sediment which has been deposited in this region.

43 This basin-scale depositional pattern suggests that pre-established basin topography can

44 have an important control on sedimentation which can impact characteristics such as

45 potential hydrocarbon storage.

46 **Keywords**: submarine channels; submarine lobes; turbidity currents; flow

47 transformation; abyssal plain; South China Sea

48 **1. Introduction**

49 Turbidity currents are particle-laden, seafloor-hugging gravity flows that move

50 downslope because of the density difference between the sediment-laden current and

51 the ambient water (Daly, 1936; Middleton and Hampton, 1973). These currents are

52 major transporters of sediment from the continental shelf to the deep ocean, where they

53 can run out for up to several thousand kilometers (Heezen and Ewing, 1952; Schwenk,

54 2004; Talling, 2014; Hunt, 2017; Heerema et al., 2020; Wells and Dorrell, 2021). The

55 deposits of these flows, called turbidites, are important as they are a potential sink for

56 organic carbon, microplastics and other pollutants (Galy et al., 2007; Azpiroz-Zabala

57 et al., 2017; Kane et al., 2019; Hage et al., 2020). These deposits can also host large

58 hydrocarbon reservoirs (Posamentier and Walker, 2006).

59 As turbidity currents flow over the seafloor they can be either net-erosive, net-

60 bypassing or net-depositional (see review in Pohl, 2019). The exact interaction with the

61   seafloor is a result of changes to their internal flow characteristics, such as velocity,

62   concentration, and thickness. However, their interaction with the seafloor can also be

63   influenced by external controls such as the degree of confinement, slope gradient and

64   substrate type, over which the turbidity current flows (Stevenson et al., 2015). On

65   continental margins, turbidity currents are typically confined within submarine

66   channels or canyons (e.g., Heezen et al. 1964; Pratson et al., 1994; Posamentier and

67   Walker, 2006; Piper and Normark, 2009; Puig et al., 2014). This confinement acts to

68   focus the flow, allowing it to maintain its competency and thus erode and transport

69   sediment over long distances (Posamentier and Walker, 2006; Stevenson et al., 2015).

70   Upon exiting these channels, turbidity currents often lose their lateral confinement,

71   triggering flow relaxation (rapid flow transformation and a lowering of maximum

72   velocity), which enhances shearing at the base of the turbidity current and leads to

73   seafloor scouring (Mutti and Normark, 1987; Palanques et al., 1996; Wynn et al., 2002;

74   Brooks et al., 2018; Pohl et al., 2019; Tinterri et al., 2020). Following flow relaxation,

75   the turbidity current is also able to entrain larger volumes of ambient water as a

76   consequence of the un-confinement (Imran et al., 2004; Pohl et al., 2019). This dilutes

77   the flow and further reduces its velocity leading to reduced competency (Imran et al.,

78   2004; Pohl et al., 2019). The loss of competency of unconfined turbidity currents results

79   in deposition of their sediment load leading to the development of widespread sediment

80   lobes (Normark, 1970; Bouma et al., 1985; Parsons et al., 2002; Posamentier and

81   Walker, 2006; Bouma et al., 2012; Talling et al., 2015; Dennielou et al., 2017; Tinterri

82   et al., 2020; Wells and Dorrell, 2021). This model of transitioning turbidity current

83   characteristics in the deep-sea from net-erosive/net-bypass to net-deposition is based in

84   part on numerous observations of channel-to-lobe transitions on the modern seafloor,

85   e.g., the Bengal Fan (Piper and Normark, 1983; Schwenk, 2004), Indus Fan (Wynn et

86   al., 2007; Kumar et al., 2019), Amazon Fan (Damuth and Kumar, 1975; Flood et al.,

87   1991; Pirmez and Imran, 2003), Congo Fan (Savoye et al., 2009; Dennielou et al., 2017;

88   Rabouille et al., 2017), and Mississippi Fan (Wynn et al., 2007), as well as in the rock

89   record, e.g., outcrops in the foreland basins of the South-Central Pyrenees, Spain (Mutti

90   and Normark, 1987), the Piedmont Basin, northwestern Italy (Mutti, 1992), the

91   Carboniferous Ross Sandstone of western Ireland (Posamentier and Walker, 2006), and

92   extensive outcrops in the Karoo Basin, South Africa (Brooks et al., 2018). This model

93   has also been supported by laboratory and numerical modelling experiments (e.g.,

94   Bowen et al., 1984; Waltham, 2004; de Leeuw et al., 2018).

95   Less common are examples were turbidity currents transition from being net-

96   depositional/net-bypassing to net-erosive. The transition from net-deposition to net-

97   erosion can result in re-channelization/re-confinement of the turbidity current and can

98   be a consequence of abrupt changes in seafloor bathymetry (Stevenson et al., 2015).

99   Previous studies have shown re-channelization of turbidity currents on delta slopes,

100   continental slopes and on continental rises. On the western Nigeria Delta, channel-to-

101   lobe-to-channel transitions have been observed associated with breaks in slope (Jobe et

102   al., 2015; 2017). Offshore Nigeria and in the Gulf of Mexico, re-channelization is

103   observed at the spill-point of mini-basins located on the continental slope (Prather et

104   al., 1998; Prather, 2003). Transitions from intra-slope lobes to channel-levee systems

105   have also been identified in the rock record from the former stepped continental slope

106   of the Karoo Basin, South Africa (Brooks et al., 2018). More distally, offshore

107   northwest Africa, re-channelization has been observed on the Agadir continental rise

108   (Wynn et al., 2002; Stevenson et al., 2013). In all cases the re-channelization observed

109   was associated with an increase in slope gradient. However, channel incision has also

110   been identified to have been a consequence of processes such as salt-tectonism (Gee

111   and Gatwathorpe, 2006).

112   Here, we aim to document a new mechanism for the re-channelization of turbidity

113   currents on abyssal plains. Using multibeam bathymetric, multichannel seismic and

114   core data from the abyssal plain of the South China Sea, we aim to show: (1) that pre-

115   existing topographic highs (seamounts and bedrock ridges) can lead to the erosion of

116   submarine channels on an abyssal plain and; (2) this re-channelization can lead to the

117   coarsening of deposits. Understanding how channel systems can be formed in abyssal

118   plain settings is important for developing models that better explain basin-floor deposits,

119   sediment dispersal and potential hydrocarbon storage in deep-water settings.

120   **2. Geological setting**

121   The South China Sea is one of the largest marginal seas of the western Pacific

122   region. The basin formed as a result of crustal rifting and subsequent drifting during the

123   late Eocene or early Oligocene to middle Miocene (Taylor and Hayes, 1980; Li et al.,

124   2014). The study site (Figs 1 and 2) is located in the north (proximal) to center (distal)

125   of the abyssal plain, extending southward (downslope) from the base of the continental

126   slope to the northern edge of the fossil spreading center with an age of 15 Ma (Li et al.,

127   2014). A number of named and unnamed submarine canyons incise the continental

128   margin, including, from west to east, the Central Canyon (Gong et al., 2011; Su et al.,

129   2014), Pearl River Mouth Canyon (Ding et al., 2013), Shenhu canyon group (Zhu et

130   al., 2010; Yin et al., 2019), Dongsha Canyon (Yin et al., 2015), Taiwan (Formosa)

131   Canyon (Ding et al., 2010), Penghu Canyon (Yu and Chang, 2002), and Gaoping

132   (Kaoping) Canyon (Liu et al., 1993) (Fig.1). These submarine canyons act as conduits

133   for the transport of large amounts of sediment from the shelf to the oceanic basin center

134   (Yin et al., 2020). As a consequence of this sediment delivery system, the South China

135   Sea abyssal plain is dominated by turbidite deposits interbedded with pelagic deposits,

136   500 to 1500 m thick (Expedition 349 Scientists, 2014; Yin et al., 2020).

137   **3. Data and methods**

138   Two multibeam bathymetric surveys and 12 multichannel seismic reflection

139   profiles are used in this study (Fig. 1). The two multibeam bathymetric surveys were

140   collected by the Second Institute of Oceanography, Ministry of Natural Resources of

141   China, onboard the Xiangyanghong 14. The first bathymetric survey, covering 97% of

142   the study area, was collected in 2005, using a RESON SeaBat 8150 multibeam system.

143   This multibeam system was operated at 12 kHz with a beam aperture of 150°, and a

144   vertical sounding accuracy of ~0.3% water depth. The second bathymetric survey,

145   covering 3% of the study area, was collected in 2014, using a Kongsberg EM122

146   multibeam system. This system was operated at 12 kHz, with a beam aperture of 150°,

147   and a vertical sounding accuracy of ~0.2% of water depth. The two sets of multibeam

148   soundings were processed using CARIS HIPS and SIPS software. Data were processed

149 to correct for differences in sound velocity in the water column, tidal level, navigation

150 and ship's motion. Combined Uncertainty and Bathymetry Estimator and "Surface

151 filter" were used to eliminate outliers in the raw sounding data (Calder and Mayer,

152 2003). The swath angle surface method in CARIS HIPS and SIPS software was used

153 to build a high-resolution seabed digital terrain model with a grid resolution of 100 m

154 and a total area of 64,500 km^2. The multibeam bathymetric data were firstly used to

155 show the general seafloor morphology of the South China Sea abyssal plain, including

156 seafloor slope gradients, significant seafloor features, as well as their size. Second,

157 detailed morphologic parameters of the submarine channel systems in the study area

158 were measured based on the multibeam bathymetric data, including orientation, length,

159 width, depth, width to depth ratio, sinuosity. Channel width and depth were measured

160 every 5 km along the channel thalweg. Third, longitudinal and transversal bathymetric

161 profiles of the submarine channels were plotted based on the high-resolution seabed

162 digital terrain model.

163   The 12 multichannel seismic reflection profiles were collected between 2004 and

164 2009, using a 480-channel seismic data acquisition system. The system has a 12.5 m

165 receiver interval, 50 m source interval, 125 m minimum offset, 2 ms sampling rate, and

166 60 folds of coverage. Seismic data were processed using a standard pre-stack time-

167 migration procedure. Major processing steps included noise reduction, deconvolution,

168 amplitude correction, trace selection, velocity analysis and model building, and time

169 migration. Seismic data have a domain frequency between 40 and 60 Hz, which gives

170 a vertical resolution (tuning thickness) of about 8 to 13 m (assuming an average interval

171   velocity of about 2000 m/s), as estimated from International Ocean Discovery Program

172   (IODP) well-logging data (Expedition 349 Scientists, 2014). These seismic profiles,

173   2040 km long in total, were used to identify large subsurface features in the study area

174   through seismic stratigraphy analysis. The seismic stratigraphic analysis was performed

175   following the conventional method and basic criteria proposed by Mitchum et al. (1977)

176   and Catuneanu et al. (2009). This method uses reflection terminations to identify

177   discontinuities and internal reflection configurations, and unit shapes to characterize

178   seismic facies.

179   Three IODP sites of sediment cores are used in this study (Fig. 1), U1431, U1432,

180   U1499. The first two sites are associated with IODP Expedition 349 executed in 2014.

181   The third site is associated with IODP Expedition 367 executed in 2017. Age-depth

182   models of the sediment cores are used to estimate age of the seismic discontinuities

183   based on the published time-depth conversion (Yin et al., 2020). Lithology of the

184   sediment cores is used to calibrate seismic facies.

185   **4. Results**

186   *4.1. General morphology of the study area*

187   The study area (Fig. 2) extends about 410 km from the foot of the continental slope

188   (water depth 3800 m) to the fossil spreading center in the abyssal plain (water depth

189   4300 m) and covers an area of 58550 km^2. The area between the continental slope to

190   the north boundary of sets of seamounts and ridges is defined as the proximal abyssal

191   plain (Fig. 2), and the area between the north boundary of sets of seamounts and ridges

192 and the fossil spreading center is defined as distal abyssal plain. The average slope

193 gradient of the study area decreases downslope, from 0.10° to 0.03°. Several high-

194 elevation features (Fig. 2) are seen in the central and southern sectors of our study area.

195 These features have two predominant shapes: blocky (i.e., seamounts; Yang et al., 2015)

196 and linear (i.e., bedrock ridges; Sibuet et al., 2016). The seamounts have an area of 50

197 to 2000 km^2 each and heights of 800 to 3700 m. The bedrock ridges are 10 to 45 km

198 long and are 50 to 500 m high, with a southwest–northeast orientation. The spacing

199 between these ridges ranges from 0 to 50 km. Submarine channels meander around the

200 seamounts and bedrock ridges in the distal abyssal plain (Fig. 2).

201   *4.2. Channel morphology*

202   The abyssal plain of the South China Sea appears featureless except for the

203 observed bedrock highs and the observed channels (Figs 2 and 3). The channel system

204 C1 (Figs 2B and 3) extends 180 km downslope originating 200 km from the end of the

205 Pearl River Mouth Canyon between the seamounts and bedrock ridges to the fossil

206 seafloor-spreading ridge. The longitudinal profile of the channel C1 changes downslope

207 from linear to slightly concave in shape (Fig. 4A). This channel is 350 to 600 m wide

208 and up to 40 m deep. The width-to-depth ratio is 35 to 575. This channel has an average

209 sinuosity of 1.15.

210   Channel C1 has two separate reaches separated by an area (45 km wide) where no

211 channel can be resolved (Figs 2 and 3). The upper reach is 1200 to 6000 m wide and 5

212 to 30 m deep. It has a channel floor gradient of 0.06° (Fig. 4A). The width-to-depth

213 ratio of the upper reach is 110 to 575. In cross-section, the upper reach is U-shaped (Fig.

214   4B). The point of origin for the upper reach is 17 km north of seamount S5. From there,

215   the channel meanders southward, closely skirting the base of seamount S3, then passing

216   between seamounts S4 and S5 over a total length of 63 km. The upper reach ends at the

217   same latitude of the southern edge of seamount S4 (Fig. 2). This reach has two courses:

218   a deeper and longer (66 km) western course that skirts the eastern edge of seamount S3

219   and a shallower and shorter (12 km) eastern course that lies between seamounts S3 and

220   S5 (Figs 2 and 3).

221   The lower reach of Channel C1 is 350 to 2700 m wide and 5 to 40 m deep, with a

222   channel floor gradient of 0° to 0.06°. The width-to-depth ratio of the lower reach is 35

223   to 500. This reach is narrower and deeper than the upper reach and the narrowest and

224   deepest position locates between the seamounts S8 and S9 (Figs 2, 3, 4A), the fossil

225   seafloor spreading center. The upstream of the upper reach is characterized by a U-

226   shaped cross-section (Fig. 4B). Downstream, the channel transitions from a wider to a

227   narrower U-shape and eventually becomes V-shaped. The lower reach starts 45 km

228   south of where the upper reach becomes unresolvable (Fig. 2), extending 123 km

229   between four seamounts, S6–S9, and more than a dozen linear bedrock ridges (Fig. 2).

230   The lower reach begins to develop 36 km south of the northern edge of seamount S7

231   and 16 km north of the seamount S6. From there, the channel meanders southward,

232   passing between seamounts S6 and S7 (approximately 21 km apart), then through the

233   field of bedrock ridges and finally the narrow 5 km gap between seamounts S8 and S9.

234   This lower reach ends in an open area between seamounts S8 and S9, which lie along

235   the fossil spreading ridge (Fig. 2). The lower reach has two courses with a length of 75

236   km (western course) and 80 km (eastern course), respectively, which merge close to the

237   north of seamount S8.

238   On both sides of channel C1, several channel-like features have developed (Fig.

239   2). Because these features have low relief and no seismic line crosses them, more

240   seismic and higher-resolution bathymetric data are required to discern these features in

241   the future.

242   *4.3. Channel-related seismic facies*

243   A regional discontinuity, H1, was identified in the shallow strata of the study area

244   (Figs 5, 6 and 7). This discontinuity, which exhibits high-amplitude reflections,

245   separates overlying high-amplitude reflections (upper seismic unit) from underlying

246   low-amplitude reflections (lower seismic unit). The age of discontinuity H1 dates to the

247   beginning of the Pleistocene (∼2.6 Ma) according to seismic–well correlations (IODP

248   Site U1431; Yin et al., 2020) and time-depth models from IODP Site U1431 (Li et al.,

249   2015). The Quaternary sediment thickness changes downslope from 200 m at the IODP

250   site U1499 at the foot of the continental slope to 150 m in the middle of the proximal

251   abyssal plain, then to 142 m in the upper reach of channel C1, further to 112 m between

252   the upper and lower reaches of channel C1, finally to 190 m in the lower reach of

253   channel C1. Channel C1 is incised into the upper seismic unit and the lowest

254   stratigraphic depth of incision is H1.

255   Six significant channel-related seismic facies were identified within the upper

256   seismic unit (Fig. 8). Lenticular seismic facies (LF) are characterized by slightly

257   concave bottom and also by lenticular seismic configurations (Fig. 8). The reflections

258   of this facies are of moderate to high amplitude and moderate continuity. The facies

259   themselves are lens-shaped, with onlaps and/or downlaps often seen along the facies

260   boundaries. The LF seismic facies spread over the open area of the distal abyssal plain

261   between the upper and lower reaches of channel C1 (Fig. 7A). Data from IODP Sites

262   U1432 and U1499 (Fig. 1) show that the lenticular seismic facies consist of greenish

263   gray clays (75% to 95%) interbedded with small amounts of clayey silt and sand, and

264   calcareous ooze and nannofossil (Fig. 9; Expedition 349 Scientists, 2014; Expedition

265   367 Scientists, 2018).

266   Channel-fill seismic facies (CF) are identified and are characterized by prominent

267   external boundaries identifiable by sudden lateral changes to seismic reflections (Fig.

268   8). These fill boundaries, which are defined by high-amplitude reflection interfaces, can

269   deeply incise underlying reflections, even down to discontinuity H1. Occurrences of

270   these seismic facies are narrow (no more than 1 km in width), with subparallel

271   reflections of moderate to high amplitude and high to low continuity. The seismic

272   profile (Fig. 6C) across the upper reach of channel C1 shows the seismic facies CF

273   include at least 11 significant cycles of incision surfaces and onlaps and draping. Theses

274   facies occur only among the seamounts and ridges in the distal abyssal plain. No IODP

275   data is available for sediments which are characterized by seismic facies CF.

276   Wedge-to-mound-shaped seismic facies (WSF) are identified and are

277   characterized by flat or slightly convex bottom and also by convergent seismic

278   configurations that thin away from the channel-fill seismic facies (Fig. 8). These facies

279   exhibit reflections of moderate amplitude and moderate to high continuity. Onlaps and

280   downlaps both occur within the facies, which are always located adjacent to the

281   channel-fill facies. The facies could appear in seafloor depressions (Fig. 6B) bounded

282   by the channel-fill seismic facies and seafloor bulges. IODP Site U1431 shows that the

283   WSF facies consist of dark greenish gray clay and clayey silt interbedded with sand and

284   nannofossil (Fig. 9; Expedition 349 Scientists, 2014).

285   The wavy seismic facies (WF) are characterized by a continuous wavy seismic

286   configuration (Fig. 8). The facies exhibit reflections of moderate amplitude and high

287   continuity. The waves of the facies are asymmetrical, with upstream flanks being

288   steeper and shorter than downstream flanks. These waves show evidence of upslope

289   (local seafloor, i.e. northeast) progradation. Their wave heights generally decrease

290   downslope (southwest) and away from the channel-fill facies, and change from small

291   to large to middle through time (Fig. 6A, B). The wavy seismic facies are typically

292   separated from the channel-fill facies by the wedge-to-mound shaped facies. The wavy

293   seismic facies lie on a slight bulge in the west of seamount S3 (Fig. 6A). The lower

294   boundary of the wavy seismic facies is discontinuity H1. No drilling data is on the

295   sediments of the seismic facies WF.

296   Transparent to chaotic seismic facies (TF) are characterized by transparent and/or

297   chaotic seismic reflections of low amplitude and low continuity (Fig. 8). The facies,

298   which exhibits an irregular shape in cross-section, are found scattered within the

299   widespread lenticular seismic facies. IODP Site U1432 shows that the seismic facies

300   TF consist of clay layers interbedded with very thinly bedded (centimeter scale) or

301   laminated silty layers (Expedition 349 Scientists, 2014; Yin et al., 2020).

302   The parallel to sub-parallel seismic facies (PF) are characterized by a parallel to

303   subparallel seismic configuration and reflections of moderate to high amplitude and

304   high continuity (Figs 5 and 8). Sometimes the reflection amplitude of the facies is a bit

305   higher at the northern flank of a seamount than in more distal areas (Fig. 10).

306   Occurrences of the parallel to subparallel seismic facies exhibit a sheeted shape and are

307   found widespread in the proximal abyssal plain between the continental slope and the

308   seamounts and ridges, but far from the channel-fill seismic facies (Fig. 6A). IODP site

309   U1431 shows that the seismic facies PF are composed mainly of clays interbedded with

310   thin silts or carbonates (Expedition 349 Scientists, 2014; Yin et al., 2020).

311   **5. Discussion**

312   *5.1. Interpretation of seismic facies*

313   The lenticular facies (LF) are interpreted as representative of lobes formed by

314   deposition from unconfined concentrated turbidity currents. This interpretation is based

315   in large part on where the facies are found, i.e. at the upper reach exit of submarine

316   channel C1 on the abyssal plain of the South China Sea (see Fig. 1 for channel locations).

317   This interpretation is supported by similar observations from other abyssal plain

318   settings, e.g., Gulf of Mexico (Dixon and Weimer, 1998; Prather et al., 1998), offshore

319   Indonesia (Saller et al., 2004), the Philippine Sea (Pickering et al., 2013), and western

320   equatorial Atlantic abyssal plain (offshore Brazil, Rimington et al., 2000; Wynn et al.,

321   2007). The moderate to high amplitude reflections of this facies are believed to

322   represent interbedded coarser (sand and silt) and finer (clay) sediments (Fig. 9;

323   Expedition 349 Scientists, 2014; Li et al., 2015).

324   The channel-fill facies (CF) occurs beneath the modern submarine channels (Fig.

325   6) that are visible in the multibeam bathymetric data. We therefore suggest that the

326   facies represent deposition within the channel system during the Pleistocene after the

327   formation of the H1 unconformity. Some CF overlie on magmatic activity zones (Fig.

328   7C, D) and the corresponding modern channel C1 extends nearby the magmatic ridges

329   (Fig. 3B), indicating that the channels may tend to choose their courses affected by the

330   underlying magmatic activity due to more erosive seabed. The channel-fill seismic

331   facies are believed to represent coarse sediments deposited by turbidity currents

332   confined within the channels. Similar coarse deposits from turbidity currents within

333   channels have been observed in other deep-water settings using drill-well data, e.g.,

334   Gulf of Mexico (Dixon and Weimer, 1998; Prather et al., 1998), and Congo basin

335   (Wang et al., 2016).

336   The wedge-to-mound-shaped facies (WSF) occur along the flanks of submarine

337   channel C1. The facies thin with distance away from the channel (Figs 6 and 8). This

338   is consistent with interpretations of similar features in other deep-water settings, e.g.,

339   Gulf of Mexico (Hackbarth and Shew, 1994; Prather et al., 1998; Beaubouef and

340   Friedmann, 2000), the WSF are therefore interpreted as muddy overbank deposits (i.e.,

341   levees, Fig. 9) formed by upper dilute turbidity currents that rode higher than the

342   channel walls and spilled out of the channel (Prather et al., 1998; Posamentier and

343   Walker, 2006). In addition, the WSF may occur in the seafloor depressions bounded by

344 slight bulges (Fig. 6A). The bulges-depressions were probably formed by seafloor

345 deformation due to local base uplift. The mild relief of the paleo-seafloor bulge-

346 depressions near the channel (Fig. 6A) also might promote the development of the WSF

347 by capturing more turbidity currents and sediments in the depressions. It indicates that

348 seafloor deformation could contribute to the development of the channel system.

349 The wavy facies (WF) could be interpreted to be seafloor deformation, i.e.

350 sediment creeps, or to be indicative of flow interaction with the sedimentary bed. If the

351 former mechanism was responsible, the older facies would exhibit larger wave heights

352 due to being subjected to a longer period of deformation. The general transition of wave

353 height from small to large to medium sizes through time indicates that the deformation

354 is unlikely to be the dominant mechanism for the formation of the observed wavy facies.

355 The facies show a series of parallel reflectors which appear to prograde upslope (Fig.

356 5B). Similar facies have been interpreted as representative of sediment waves which

357 have resulted from the repeated passage of supercritical flows (e.g., Normark et al.,

358 1980; Flood, 1988; Migeon et al., 2000; Wynn and Stow, 2002; Cartigny et al., 2011;

359 McCave, 2017). The NW-SE orientation and NE migration of the sediment waves (Figs

360 3A and 6B) suggest that unconfined turbidity currents responsible for the sediment

361 wave formation should come from north and/or northeast, the direction of the northern

362 SCS continental margin with large canyons (Fig. 1). The higher average slope gradient

363 of the sediment wave field (Fig. 6A, B) may allow turbidity currents to accelerate and

364 thus erode seafloor substrate. This increase in velocity and sediment entrainment is

365 likely to be conducive to the formation of the supercritical flow bedforms (Cartigny et

366 al., 2011, Symons et al., 2016; Slootman and Cartigny, 2020).

367   The sporadically occurring transparent to chaotic facies (TF) have been commonly

368 interpreted elsewhere in deep-water settings as fluid migration pathways (Judd and

369 Hovland, 2007; Sun et al., 2012; Yin et al., 2020), submarine channel fills (Posamentier

370 and Walker, 2006; Bellwald et al., 2020) or mass transport deposits (Hackbarth and

371 Shew, 1994; Prather et al., 1998; Posamentier and Walker, 2006; Moscardelli and

372 Wood, 2008; Alfaro and Holz, 2014). In our study area, there is no significant indication

373 of fluid migration (i.e., no fluid migration pathway connecting these overlying seismic

374 facies to a deeper fluid source). The scale of the seismic facies is similar to the identified

375 submarine channels. However, the seismic profile 40 km north of seismic facies TF

376 shows no significant evidence of submarine channels being present (Fig. 5A).

377 Therefore, it is unlikely that palaeo-submarine channels are responsible for the

378 observed facies. Furthermore, there is no resolvable evidence of channel-overbank

379 deposition (e.g., WSF) beside seismic facies TF, that would be present if submarine

380 channels were responsible (Fig. 5C, D). We therefore believe that it is unlikely that

381 submarine channels are responsible for the formation of these seismic facies. A number

382 of studies have identified the occurrence of mass transport events around the margins

383 of the South China Sea (Wang et al., 2013; Sun et al., 2017). These observations have

384 therefore led us to interpret the transparent to chaotic facies as mass transport deposits

385 which probably come from nearby seamounts and ridges.

386   Within the parallel to subparallel (PF) seismic facies, the configuration of

387 reflections (parallel to subparallel) indicates a spatially uniform sedimentation rate

388 (Sangree and Widmier, 1977; Hackbarth and Shew, 1994). As calibrated by drilling

389 data from IODP Site U1431, the seismic facies are composed mainly of clays

390 interbedded with thin silts or carbonates (Fig. 6. Expedition 349 scientists, 2014; Li et

391 al., 2015; Yin et al., 2020). In deep marine environments, fine clays are probably the

392 result of pelagic deposition or very dilute unconfined turbidity currents (e.g., Prather et

393 al., 1998; Rothwell et al., 1998; Higuchi et al., 2007; Gennaro et al., 2013; Pickering et

394 al., 2013). The thin silts and carbonates were likely deposited by less dilute unconfined

395 turbidity currents (e.g., Prather et al., 1998; Rothwell et al., 1998; Higuchi et al., 2007;

396 Gennaro et al., 2013; Pickering et al., 2013). Thus, the parallel to subparallel seismic

397 facies are interpreted as pelagic sediments interlayered with a variable content of thin

398 turbidites.

399   *5.2. Abyssal plain depositional system*

400   The observed morphology and seismic facies suggest a depositional system that

401 extends from the base of the continental slope and across parts of the abyssal plain to

402 the fossil spreading center, encompassing a typical (proximal) pelagic deposits mixed

403 with very dilute unconfined turbidity current deposits and an unusual (distal)

404 channelized system (Fig. 11). Here we consider two processes that could have

405 contributed to the formation of this distal channelized system.

406   First, the observed depositional system could consist of the remains of a paleo-

407 channel system. In this model, the channels on the modern seafloor are the remnants of

408   old channels that have not yet been completely filled/buried by subsequent deposition.

409   However, seismic profiles across the area upslope of the exposed channels, in the

410   proximal abyssal plain, show no filled large Quaternary channels that would have fed

411   the observed channels in the south of the study area. The occurrence of the widespread

412   seismic facies PF and sporadic TF in the proximal abyssal plain indicates that pelagic-

413   dilute turbidity current mixed deposition dominates this area, accompanied by local

414   mass transport deposits (Fig. 5; Yin et al., 2020). The generally similar sediment

415   thickness in the upper stream of the channel C1 and its upper reach also indicates that

416   there would be no lobes with a much higher sediment rate in the upper stream of the

417   channel C1. A significant gap therefore exists between the source of paleo-flows (the

418   continental slope canyons) and the distal abyssal plain channels through which they

419   would have flowed. Therefore, unless significant bypass occurred (Stevenson et al.,

420   2015), this paleo-channel model is not consistent with observations from the study area.

421   Moreover, the Quaternary sediment thickness changes downslope from 200 m at IODP

422   site U1499 at the foot of the continental slope to 150 m (assuming an average interval

423   velocity of about 2000 m/s) in the middle of the proximal abyssal plain then to 142 m

424   in the upper reach of the channel C1 (Figs 5–7, 9). The thick Quaternary deposition

425   also indicates an absence of significant bypass in the northern (proximal) abyssal plain.

426   Second, the depositional (mixed pelagite-turbidite deposition) and erosional

427   (channel) system was formed by turbidity currents sourced from the confining

428   submarine canyons of the continental margin. In this model, the turbidity currents

429   become unconfined and dilute when they emerge from the canyons to flow across the

430   nearly featureless proximal abyssal plain. These flows are then subsequently re-

431   confined resulting in incising into the seafloor and formation of the observed abyssal

432   plain channels. If this interpretation is correct, the turbidite system in the study area

433   differs significantly from the classical turbidite depositional model, which describes a

434   downslope transition from confined to unconfined turbidity current deposition, without

435   subsequent re-confinement (Richards et al., 1998; Bouma, 2000; Posamentier and

436   Walker, 2006; Pohl et al., 2019). It would also be evidence of an additional mechanism

437   by which re-channelization can occur in addition to those observed in other settings

438   (e.g. Prather, 2003; Jobe et al., 2017; Brooks et al., 2018).

439   *5.2.1. Channel incision mechanisms*

440   Two possible causes are considered for the development of the observed channels

441   by turbidity currents in the area seaward of unconfined flow. First, channel incision

442   may be related to abrupt increases in slope gradient, which would result in acceleration

443   of turbidity currents, thus allowing for erosion and incision of the submarine channels

444   (Bagnold, 1954; Komar, 1973; Posamentier and Walker, 2006; Gamberi and Rovere,

445   2011; Heerema et al., 2020). However, in our study area, the abyssal plain slope

446   gradient decreases (0.10° to 0.03°). Moreover, the slope gradient decreases from 0.08°

447   to 0.06° at the head of channel C1 (Fig. 4A). Although the slope gradient increases from

448   0.04° to 0.06° at the head of the lower reach of channel C1 (Fig. 4A), the deepest

449   channel with largest width to depth ratio appears near the end of the channel course

450   where the slope gradient is almost 0° (Fig. 4A). It means that slope gradient is not the

451   dominant factor that controls channel incision in this study area. We therefore suggest

452   that abrupt increases in slope gradient are not responsible for the observed turbidity

453   current transition from depositional to erosive.

454   Second, channel development may have resulted from the interaction of turbidity

455   currents with pre-existing topography. At the northern end of the study area, where

456   widespread deposition is observed and channels are absent, the proximal abyssal plain

457   is open and largely featureless (Fig. 2). To the south, however, a number of seamounts

458   are found which are ≥5 Ma in age (Wang and Wu, 1984; Yan et al., 2008; Xia et al.,

459   2018; Jiang et al., 2019 Yin et al., 2020). The deepest base of the channel system

460   (discontinuity H1; Figs 4 and 5) dates to the beginning of the Pleistocene (~2.6 Ma)

461   (Fig. 9; Li et al., 2015; Yin et al., 2020). These dates indicate that the topographic

462   features existed prior to the development of the channel system. It is therefore likely

463   that this pre-existing topography has played a role in the development of the abyssal

464   plain sedimentary system. We now consider two possible types of current–topography

465   interaction that could have contributed to that role: current acceleration and reflection.

466   *5.2.2 Turbidity current acceleration*

467   Southward flow of previously unconfined dilute turbidity currents entering the

468   region characterized by scattered seamounts and bedrock ridges, is likely to refocus the

469   flow. According to the flux conservation principle (Komar, 1969, 1973), the

470   confinement would lead to increases in flow density and velocity between topographic

471   highs. This acceleration enhances the ability of the turbidity currents to erode and

472   entrain sediment (Bagnold, 1954; Komar, 1973). The resulting enhanced erosion could

473   therefore lead to the incision of the observed channels. Support for this envisaged

474   process is found in the fact that channels are deepest (30 – 40 m, compared with 10 –

475   20 m elsewhere) where they flow through the narrowest gaps between the seamounts

476   (S3 and S5, 10 km apart; S8 and S9, 5 km apart) (Figs 2, 3, 4A). These differences

477   suggest that the greater the lateral confinement the more erosive turbidity currents in

478   those areas become (Komar, 1973).

479   The discontinuity of channel C1 also suggests the importance of confinement to

480   turbidity current characteristics. Channel C1 is no longer resolvable after it exists the

481   gap between seamounts S4 and S5 (Fig. 2). Here, the turbidity current becomes less

482   confined (seamounts S4 and S6 are separated by ∼63 km). Reduced confinement is

483   suggested to result in a reduction in the ability of turbidity currents to erode the seafloor

484   as they entrain more ambient water and therefore dilute (Komar, 1969, 1973). As a

485   consequence of the observed loss of confinement, after passing S4 and S5, if a channel

486   has been incised it is insufficiently deep to be resolved on our bathymetry. However, it

487   is more likely that sediment has been deposited between the upper and lower reaches

488   of channel C1 (Figs 2 and 7A). Re-confinement of the turbidity current between

489   seamounts S6 and S7 results in the flow accelerating again and it is therefore able to

490   erode the seafloor and initiate the lower reach of channel C1. The continuity of the

491   observed channels therefore appears to be dependent on the degree of continued

492   confinement afforded by topographic highs.

493   *5.2.3 Reflection*

494   In addition to confining turbidity currents, the pre-existing topographic highs also

495   have the potential to result in turbidity current reflection (Hiscott and Pickering, 1984;

496   Alexander and Morris, 1994; Edwards et al., 1994). Three main types of resulting flow

497   behavior could significantly influence local sedimentation: the formation of standing

498   billows, the generation of standing waves, and flow deceleration.

499   A reflected turbidity current could interact with the original current to form

500   standing billows (mixing vortices), thus generating rapid local and uneven deposition

501   nearby the upslope side of topographic highs (Alexander and Morris, 1994). In the

502   vicinity of seamounts S5, S6, S8 and S9, where seismic lines cross from north to south,

503   sediment thickness doesn't rapidly decrease northward as away from the northern

504   (upstream) foot of this seamount (e.g., Fig. 10) except for seamount S9 (Fig. 7C).

505   Sediment is thicker at the northern foot of seamount S9 than the area surrounding site

506   U1431. The thicker sediment could be deposited by the unconfined turbidity currents

507   and their reflections, which spilled over the nearby channel C1. The reason why

508   seamount S9 shows the effect of reflected turbidity current might be that there are

509   turbidity currents with larger volume and/or higher concentration near the northern foot

510   of this seamount. These observations suggest that standing billows generated by

511   reflected turbidity currents may have contributed to deposition on the upslope side of

512   the seamounts in the study area when the turbidity current volume and concentration is

513   sufficient.

514   A reflected turbidity current could also form internal waves on the upstream sides

515   of seafloor highs (Edwards et al., 1994) resulting in the deposition of sediment waves

516   (Karl et al., 1986; Reeder et al., 2011; Droghei et al., 2016; Ribo et al., 2016). On the

517   northern (upstream) sides of the seamounts and bedrock ridges of this study, the seismic

518 profiles show no such wavy bedforms (sediment waves), except the sediment waves

519 near the northern foot of seamount S4 (Figs 2A and 6A). The northwest-southeast

520 orientation and the decrease of wave heights and wavelengths toward southwest (Figs

521 2A and 6A) indicate that the current that generates these sediment waves should come

522 from northeast. The orientation of these waves relative to the direction from which

523 turbidity currents are expected to originate and the obtuse angle of which these would

524 be reflected suggests that these bedforms are unlikely to be a consequence of

525 propagating and waning internal waves.

526   A reflected turbidity current could also be expected to slow down the original

527 (incident) current. The seismic profile across seamount S6 does show higher-amplitude

528 seismic reflections locally at the northern base of the seamount, with amplitudes

529 decreasing away from the seamount (Fig. 10). High seismic reflection amplitudes in

530 deep sea sediments commonly indicate a higher content of relatively coarse sediment

531 (e.g., Prather et al., 1998; Saller et al., 2004; Posamentier and Walker, 2006; Pickering

532 e al., 2013). This may therefore suggest that relatively coarse-grained turbidites among

533 the seamounts have been preferentially deposited locally on the north side of seamount

534 S6. This interpretation would be consistent with the scenario of a turbidity current

535 reflecting off the northern seamount wall, resulting in a reversal of flow direction or a

536 decrease of flow velocity, and the settling of relatively coarse-grained sediments onto

537 the seabed.

538 *5.3. Implications for flow re-channelization*

539   Turbidity current re-channelization systems are increasingly being documented in

540 disparate settings around the world by multibeam bathymetric and seismic data (Prather

541 et al., 1998, 2012; Gee and Gatwathorpe, 2006; Stevenson et al., 2013) and also in rock

542 outcrop studies (Mutti and Normark, 1987; Mutti, 1992; Posamentier and Walker,

543 2006; Brooks et al., 2018; Tinterri et al., 2020). First, depositional-to-erosional

544 transitions have been recognized as a consequence of salt-tectonism resulting in

545 confinement/un-confinement of channels and abrupt changes to slope gradient (e.g.

546 Gee and Gatwathorpe, 2006). Second, they have been recognized as a consequence of

547 an increase in slope gradient associated with turbidity currents spilling out of

548 sedimentary basins (e.g. Prather et al., 1998; Hunt et al., 2011; Stevenson et al., 2013).

549 Where pre-existing channel features are present these are maintained or consolidated

550 by continued turbidity current activity (Stevenson et al. 2013). Where no channel exists,

551 they can be incised by turbidity currents. Third, depositional-to-erosional transitions

552 have been shown to develop where there are significant changes to continental slope

553 gradients; lower gradients resulting in turbidity current transport capacity being

554 reduced and therefore deposition before subsequent gradient increases result in

555 turbidity current acceleration and channel incision (Prather et al., 2012; Brooks et al.,

556 2018; Jobe et al., 2017). Here, we identify an additional turbidity current re-

557 channelization mechanism.

558   Our data show that pre-existing topography, such as seamounts, located on abyssal

559 plain floors are capable of causing sufficient re-focusing of turbidity currents to enable

560   erosion and re-channelization to occur (Fig. 11). It also shows that this can occur

561   unaccompanied by increases in seafloor gradient which have been commonly been

562   identified elsewhere (Prather, 2003; Gee and Gatwathorpe, 2006; Prather et al., 2012;

563   Stevenson et al., 2013; Brooks et al., 2018). Most published deep-sea examples of

564   turbidity current re-channelization occur in small-scale submarine aprons or intra-slope

565   mini-basins of the continental slope (Gee and Gatwathorpe, 2006; Prather, 2003;

566   Prather et al., 2012; Brooks et al., 2018), which are very different from our study of an

567   open abyssal plain. One comparable system is the Agadir turbidite system on the

568   continental rise of the North-West African margin where re-channelization occurs.

569   Here, the continental shelf is <35 km wide (Wynn et al., 2002; Stevenson et al., 2013)

570   and seamounts (<500 m high, <50 km^2 in area) can be seen sporadically. The Agadir

571   system is fed by the Sous River which has a drainage area of 16,000 km^2. Sediment is

572   delivered by the Agadir Submarine Canyon which emerges onto the Agadir Basin.

573   Seaward of the Agadir Basin, the Madeira Channels act as conduits for sediment (mud

574   and fine sand) to the deep-sea (Wynn et al., 2002; Stevenson et al., 2013). The heads

575   of the Madeira Channels are ~300 km away from the Agadir Canyon mouth. They are

576   <20 m deep and <5 km wide (Stevenson et al., 2013). Turbidity currents which are re-

577   channelized within the Madeira Channels are estimated to transport >100 km^3 with a

578   frequency of 12 ka to 60 ka (Wynn et al., 2002). All these large turbidity currents

579   occurred at oxygen isotope stage boundaries (Wynne et al., 2002). In the case of the

580   South China Sea, sediment is supplied by the Pearl River Mouth Canyon and Shenhu

581   Canyon Group. At the mouth of these canyons, the abyssal plain of the South China

582   Sea opens out before the observed seamounts (<3500 m high, <2000 km^2 area) and

583   ridges (<500 m high, <45 km long, <50 km spacing) constrict the abyssal plain and lead

584   to the formation of the observed channels. In the distal abyssal plain with the observed

585   channel, sediment out of the channel consists of pelagic clay and turbidite silt and sand

586   (Fig. 9). Turbidites deposited at the mouth of the Pearl River Mouth Canyon show about

587   a frequency of 17.9 ka during the past 1 million years (Su and Zhong, 2020).

588   Comparison of these two systems does suggest that a large river-canyon system is

589   probably necessary to provide sufficient coarser sediment (sand and silt) for large

590   volume turbidity currents for re-channelization after long run out, although our study

591   area lacks of numerous sediment cores to estimate individual turbidity current volume.

592   The large volume turbidity currents are infrequent and the frequency of them is between

593   ten to tens of thousands of years. The large volume turbidity currents for re-

594   channelization may occur at periods between glacial and interglacial conditions, when

595   eustatic sea level was either rising or falling rapidly (Wynn et al., 2002). It does also

596   suggest that the re-channelized channels are shallow (dozens of meters) and narrow

597   (several kilometers). The different dominant re-channelization mechanisms in two

598   cases include emergence of sets of large-scale seamounts and ridges in the very gentle

599   abyssal plain in our study, and slope gradient increase (at least 0.04°, Stevenson et al.,

600   2013) in the smooth and open continental rise in the Agadir system.

601   The channel C1 appears to be a persistent feature during the Pleistocene (Figs 6

602   and 7). The CF seismic facies within channel C1 show at least 11 cycles of re-

603   channelization (Fig. 6C), characterized by incision surfaces, and infill characterized by

604 onlaps and draping geometry of the reflections. Cycles of channelization may be related

605 to changes in turbidity current magnitude-frequency. Large volume turbidity currents

606 may be able to transport sediment for longer distances. The larger events are likely to

607 be able to incise into the seafloor and thus erode the observed channels. However, when

608 turbidity current volumes are smaller or these flows are less frequent, sediment may be

609 deposited in these channels leading to the observed infill. Pelagic and hemipelagic

610 sedimentation will further contribute to the infill. The observed channelization/infill

611 cycles may therefore be reflective of long-term changes to sediment supply to the basin.

612 *5.4. Implications for global distributions of coarse-grained sediment*

613 This study has significant implications for understanding sedimentary deposits in

614 abyssal plain settings. Data from IODP Sites U1431, U1432 and U1499 show that over

615 the past 0.9 Ma, deposits have coarsened significantly between the proximal abyssal

616 plain and the distal abyssal plain associated with the observed channels. In the proximal

617 abyssal plain (U1432, U1499), the sand, silt and carbonate content is between 5 to 25%.

618 Near the identified channel (U1431), this content increases to 64%. This data therefore

619 suggests that turbidity currents have been able to transport larger grain sizes within the

620 regions of bedrock highs, seamounts and greater confinement, even in oceanic abyssal

621 plains. This data further supports our contention that confinement has led to increased

622 erosive capacity of turbidity currents in this area (Bagnold, 1954). These observations

623 therefore show the importance of recognizing pre-existing topography at the time of

624 deposition for anticipating deposit characteristics in deep-water settings.

625   These new observations also have important implications for hydrocarbon

626   exploration. These new South China Sea data show that the distal abyssal plain can (a)

627   have more sand-rich sediments than the proximal abyssal plain and (b) be a potential

628   exploration target in areas where a series of funneling topographic highs (e.g.,

629   seamounts and bedrock ridges) is present. Understanding the sediment dispersal

630   patterns of this basin-scale turbidity current re-channelization system is also useful for

631   developing a better understanding of source-to-sink processes.

632   **6. Conclusions**

633   Based on multibeam bathymetric and seismic reflection data tied to three IODP

634   well controls from the abyssal South China Sea, we document a new mechanism of

635   turbidity current re-channelization. Our data show turbidity currents, sourced from

636   continental slope canyons, which have travelled at least 200 km unconfined across an

637   abyssal basin plain, can erode seafloor channels as a consequence of topographic high

638   (seamounts and bedrock ridges) induced confinement. Importantly, this data shows that

639   confinement is sufficient to induce seabed erosion and does not require increases in

640   slope gradient. The contrasting flow regimes associated with confinement and un-

641   confinement lead to distinct regions of erosion, i.e. the development of channels, and

642   deposition of sediment. Moreover, we show that channel depth is dependent on the

643   degree of confinement, i.e. greater confinement leads to deeper channels.

644   The impacts on the ability of turbidity currents to erode and transport sediment

645   across the South China Sea abyssal plain of pre-existing topography are also reflected

646   by recovered sediment deposits. In comparison with the proximal abyssal plain, the

647   sedimentary deposits in the distal abyssal plain within the area of the seamounts and

648   the turbidity current channels are between three and 13 times richer in coarser

649   sediments. This supports the hypothesis that confinement has increased the flow

650   competency allowing turbidity currents to carry larger volumes of coarse sediment to

651   be deposited in this region. Recognition of the possible contrasts in deposits associated

652   with pre-existing topography in abyssal plain settings has further implications for the

653   preferential deposition and burial of organic carbon (Hage et al., 2020) and pollutants,

654   such as microplastics (Pohl et al., 2020), which can be heavily influenced by grain size.

655   Our study also indicates that distal abyssal plain of the appropriate layout (i.e., a

656   series of confining topographic highs downslope from an area of turbidity current

657   generation) could be potential hydrocarbon exploration targets.

672

673

Figure captions

Fig. 1. Study area with data used in this study, including multibeam bathymetric (red

lines), seismic (white lines), and IODP sites (black dots). *CC* = Central Canyon, *PRMC*

= Pearl River Mouth Canyon, *SCG* = Shenhu canyon group, *DC* = Dongsha Canyon,

*TC* = Taiwan Canyon, *PC* = Penghu Canyon, *KC* = Kaoping Canyon.
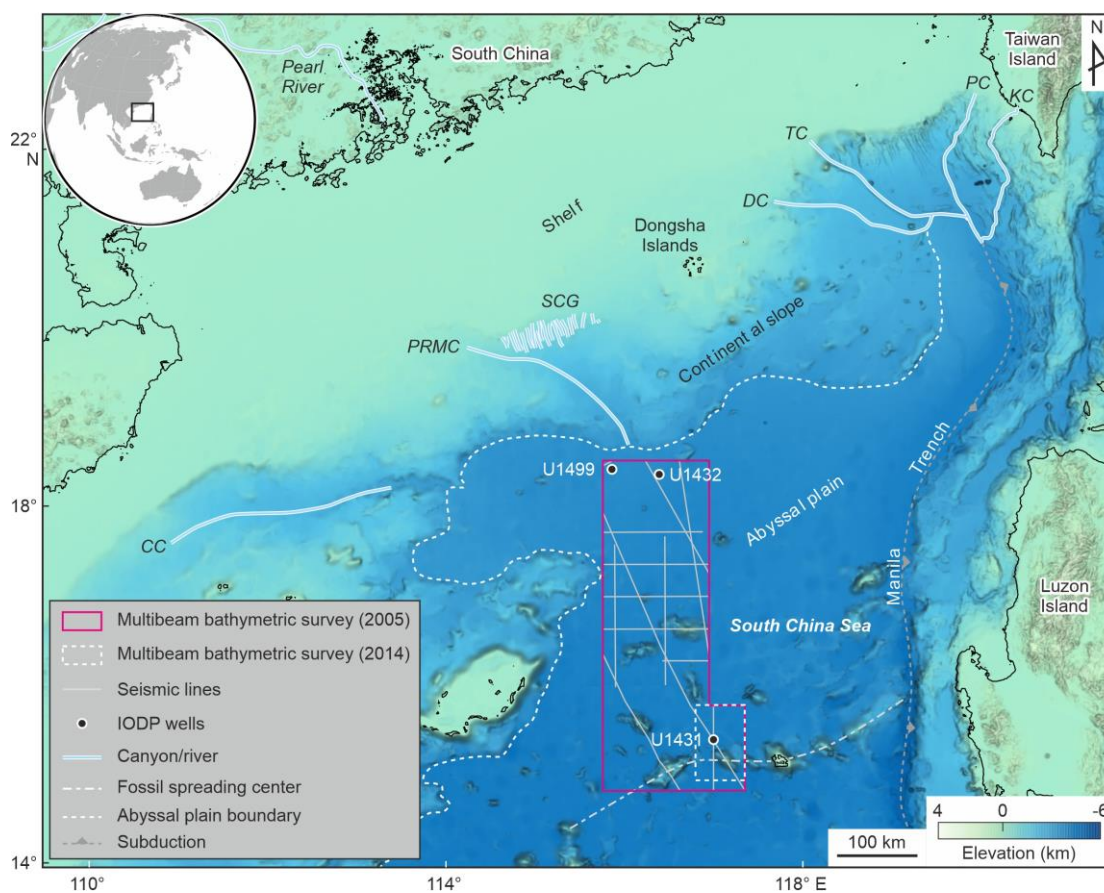
681 **Fig. 2**. Multibeam bathymetric map (**A**) and interpreted morphosedimentary map (**B**)

682 of the study area, including channels and distributaries. Black dots mark the IODP

683 drilling sites. On panel (A), red dotted line marks the location of the longitudinal profile

684 shown in Fig. 4A, yellow lines mark the locations of cross sections (labeled CS) shown

685 in Fig. 4B, and white lines mark the seismic profiles shown in Figs 5, 6, 7 and 10. On

686 panel (B), the numbers in parentheses give the ages of the seamounts (labeled S) in

687 millions of years. These ages are taken mainly from Wang and Wu (1984), Yan et al.

688 (2008), Xia et al. (2018), and Jiang et al. (2019).
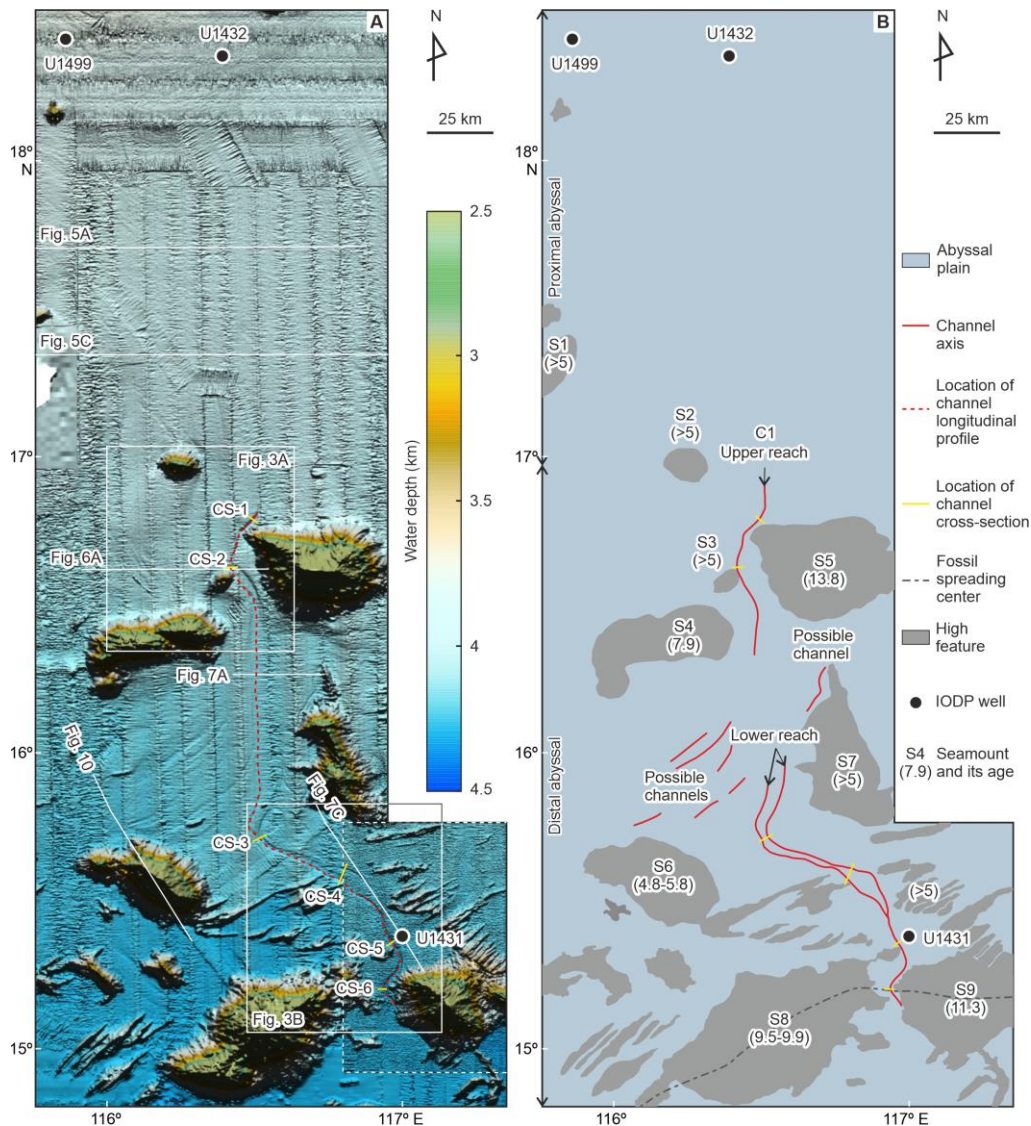
689
690

691   **Fig. 3**. Close up of the multibeam bathymetry in the upper (**A**) and lower (**B**) reaches

692   of the channel C1. While lines mark the locations of seismic profiles in Fig. 6A and 7C.

693   The black dot marks the location of IODP site U1431. Map locations are shown in Fig.

694   2A.
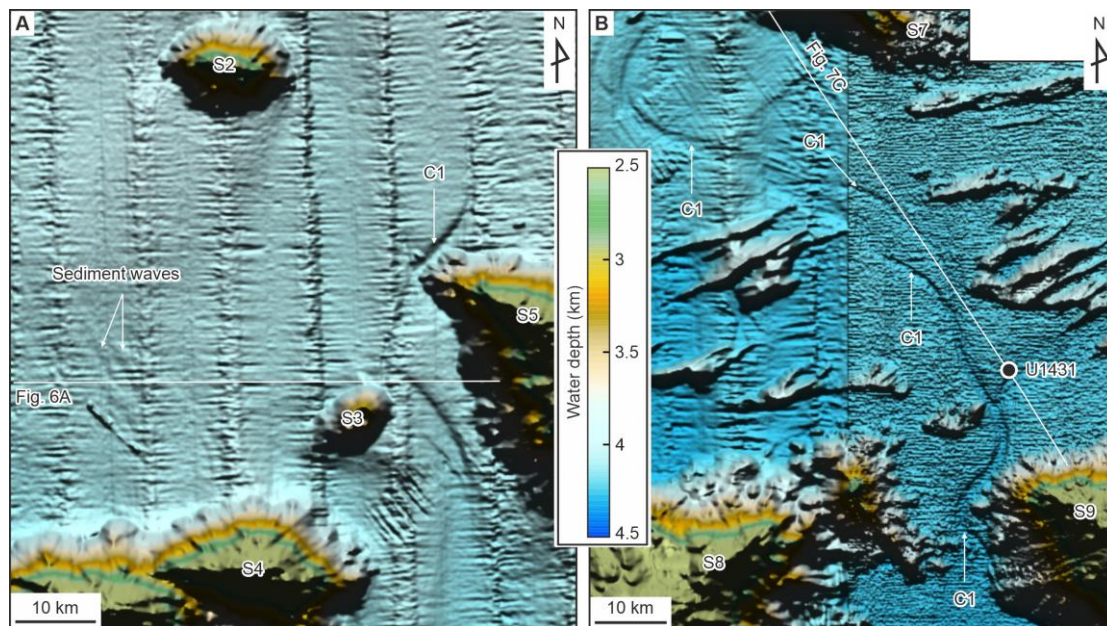
695
696

697 **Fig. 4**. Channel C1 longitudinal (**A**) and cross (**B**) sections. Channel width, depth,

698 width-depth ratio, slope gradient along the channel axis are also shown in (A). The

699 longitudinal profile was the smoothed trend of the raw data in order to avoid noise

700 interference. Cross sections CS1 and CS2 are located in the upper channel reach, and

701 cross sections CS3 through CS6 are in the lower reach. Locations are shown in Fig. 2A.
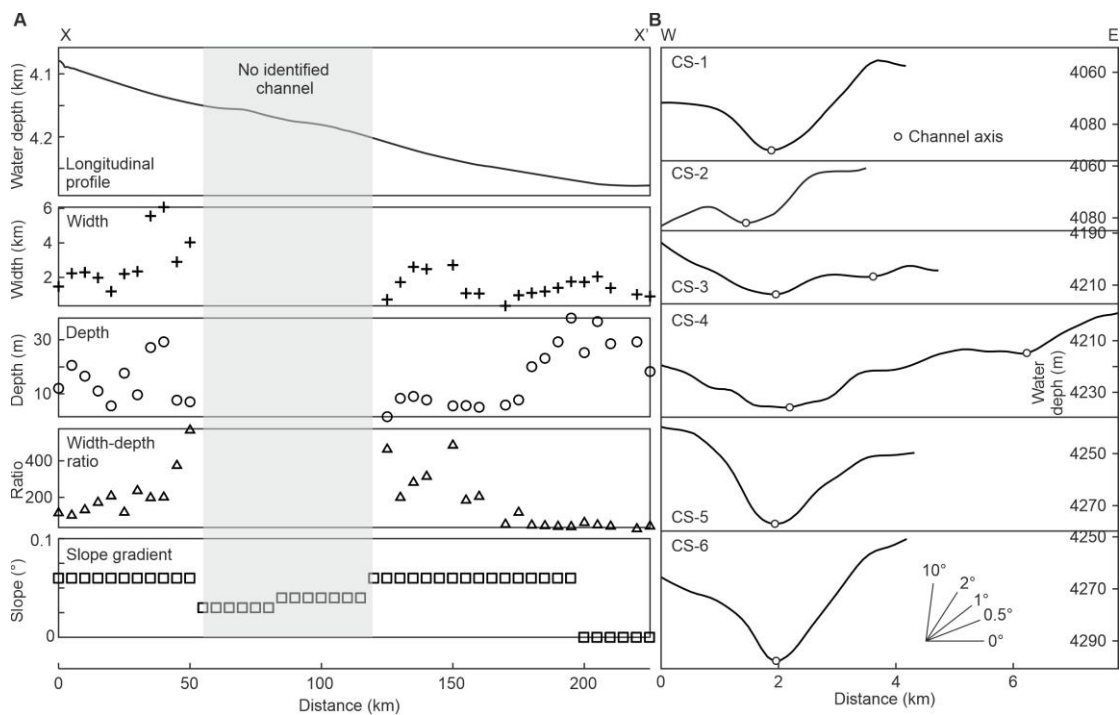
702
703

704 **Fig. 5**. Seismic profiles and interpretations in the upstream (north) of the channel C1

705 showing parallel to subparallel seismic facies (**A**) and (**B**) dominated the open abyssal

706 plain. Transparent to chaotic facies (**C**) and (**D**) are scattered in this area. PF = parallel

707 to subparallel facies. S = seamount. TWT = two-way time. Same as below. Profile

708 locations are shown in Fig. 2A.

709

710
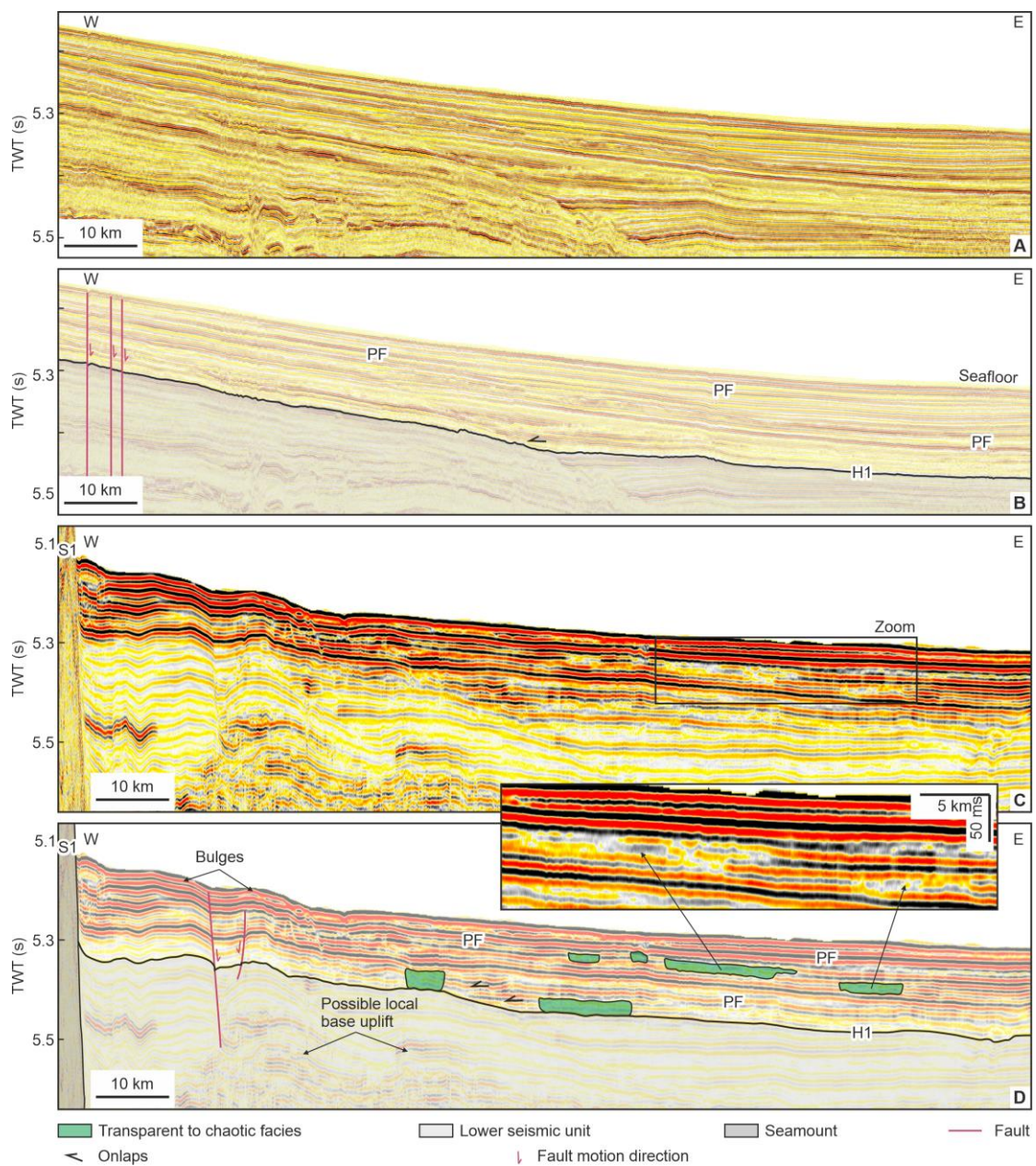
711 **Fig. 6**. Seismic profiles and interpretations across the upper reach of the channel C1

712 showing the channel at the entrance to the seamount area (**A**) and (**B**). Closeup of the

713 channel is shown in (**C**). WSF = wedge-to-mound shaped facies, WF = wavy facies, PF

714 = parallel to subparallel facies. C1 = channel C1, S = seamount. Profile locations are
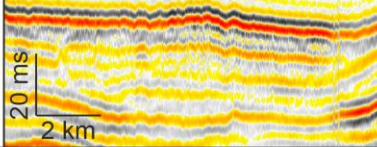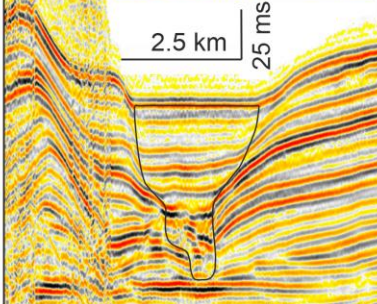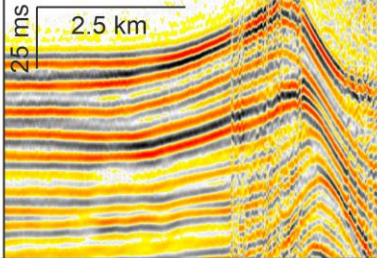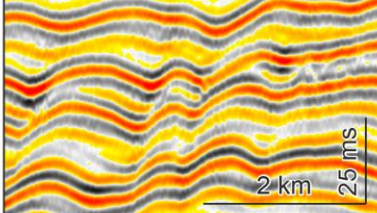
715 shown in Fig. 2A.

716
717
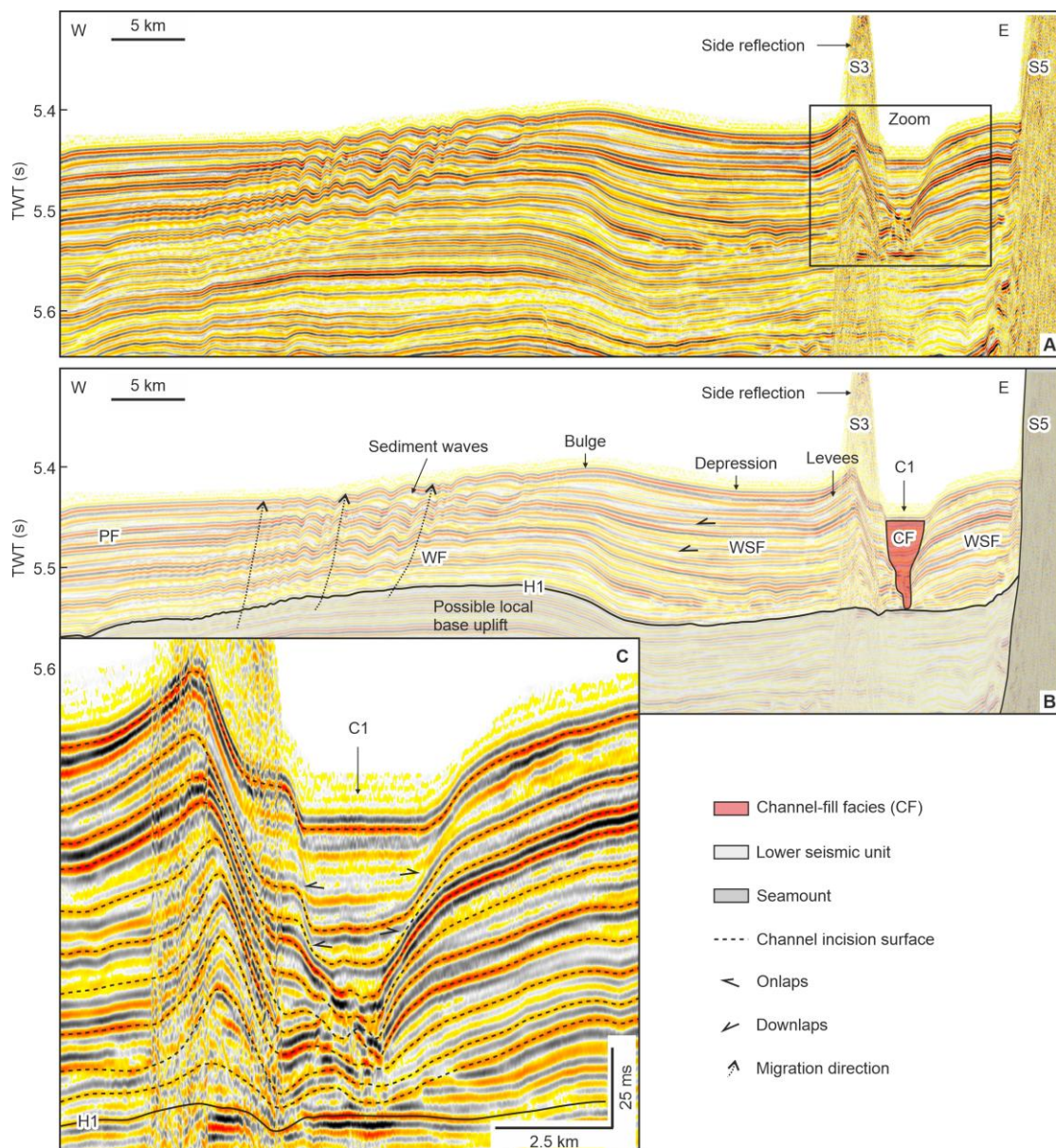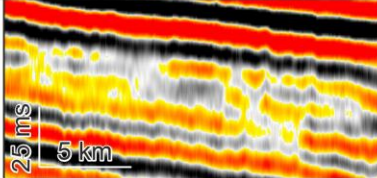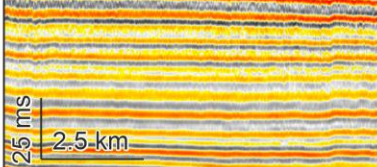
Fig. 7. Seismic profiles and interpretations between the upper and lower reaches of the

719 channel C1 (**A**) and (**B**) showing the lobes on the plain, and across the lower reach of

720 the channel C1 (**C**) and (**D**). LF = lenticular facies, PF = parallel to subparallel facies,

721 WSF = wedge-to-mound shaped facies. C1 = channel C1, S = seamount. The vertical

722 black line in (**D**) marks the location of the IODP Site U1431. Profile locations are

723 shown in Fig. 2A.
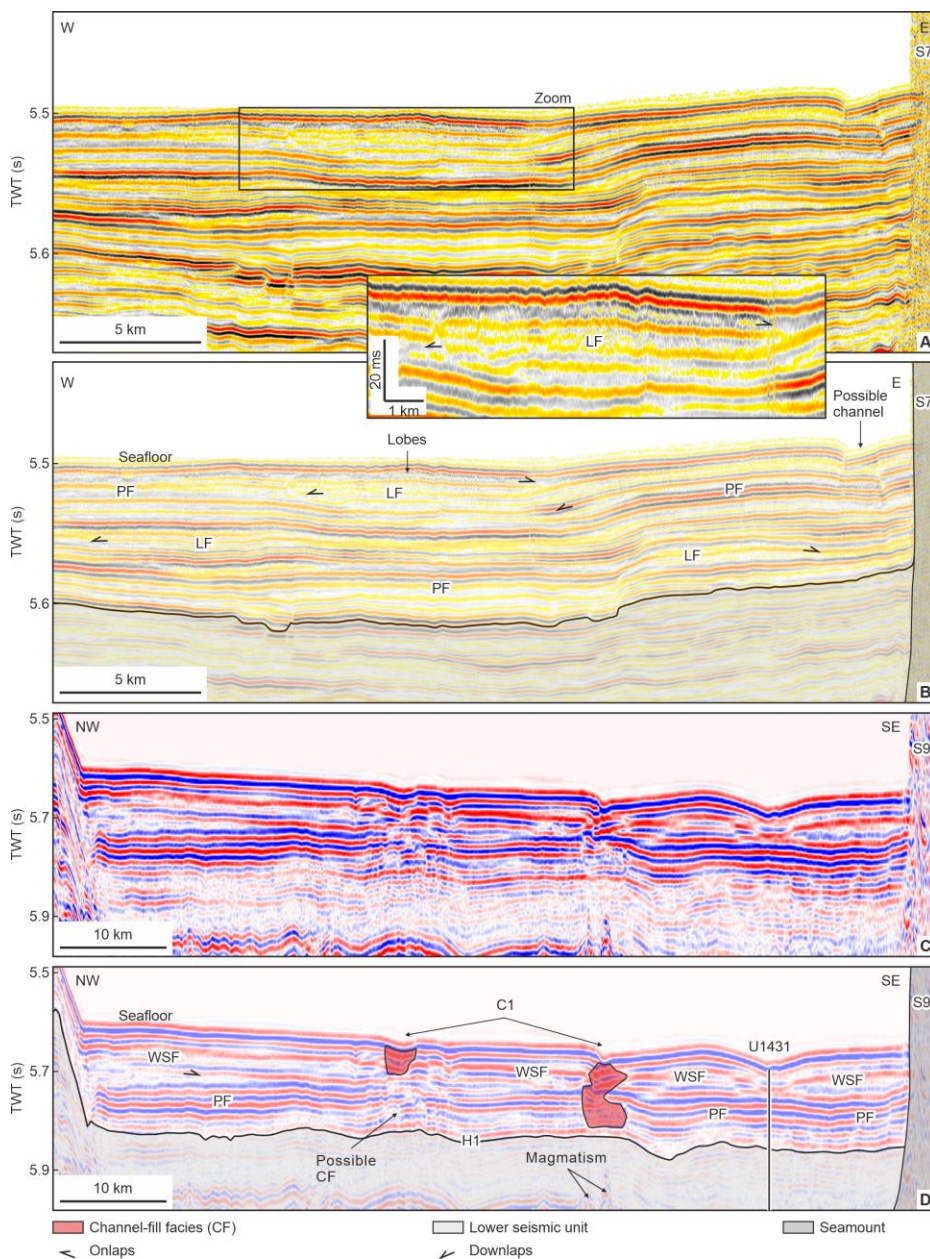
724

725

726 **Fig. 8**. The six seismic facies identified in the seismic reflection profiles, including

727 seismic examples, seismic character, and interpretation.

| Seismic facies	Examples	Seismic character	Interpretation
Lenticular (LF)		Concave bottom, lenticular configuration, moderate to high amplitude, moderate continuity, lens shape	Lobes formed by deposition from unconfined concentrated turbidity currents
Channel-fill (CF)		Channel-like external boundary, subparallel configuration, moderate to high amplitude, high to low continuity	Deposition within channels from confined turbidity currents
Wedge-to-mound-shaped (WSF)		Wedge to mound shape, flat bottom, convergent configuration, moderate amplitude, moderate to high continuity	Overbank deposits formed by dilute turbidity currents that spilled out of channels
Wavy (WF)		Continuous wavy configuration, moderate amplitude, high continuity, upslope migration	Sediment waves formed by unconfined supercritical turbidity currents
Transparent to chaotic (WF)		Transparent to chaotic configuration, low amplitude, low continuity, irregular shape	Mass transport deposits
Parallel to subparallel (PF)		Parallel to subparallel configuration, moderate to high amplitude, high continuity, sheeted shape	Mixed pelagic and unconfined dilute turbidity current deposition

728
729

730   **Fig. 9**. Lithology of the study area depositional system, as seen at IODP Sites U1432,

731   U1499 and U1431. WSF = wedge-to-mound shaped seismic facies. PF = parallel to

732   sub-parallel seismic facies. LF = lenticular seismic facies. mbsf = meters below

733   seafloor. Locations of the IODP sites and the seismic line can be seen in Fig. 2A.
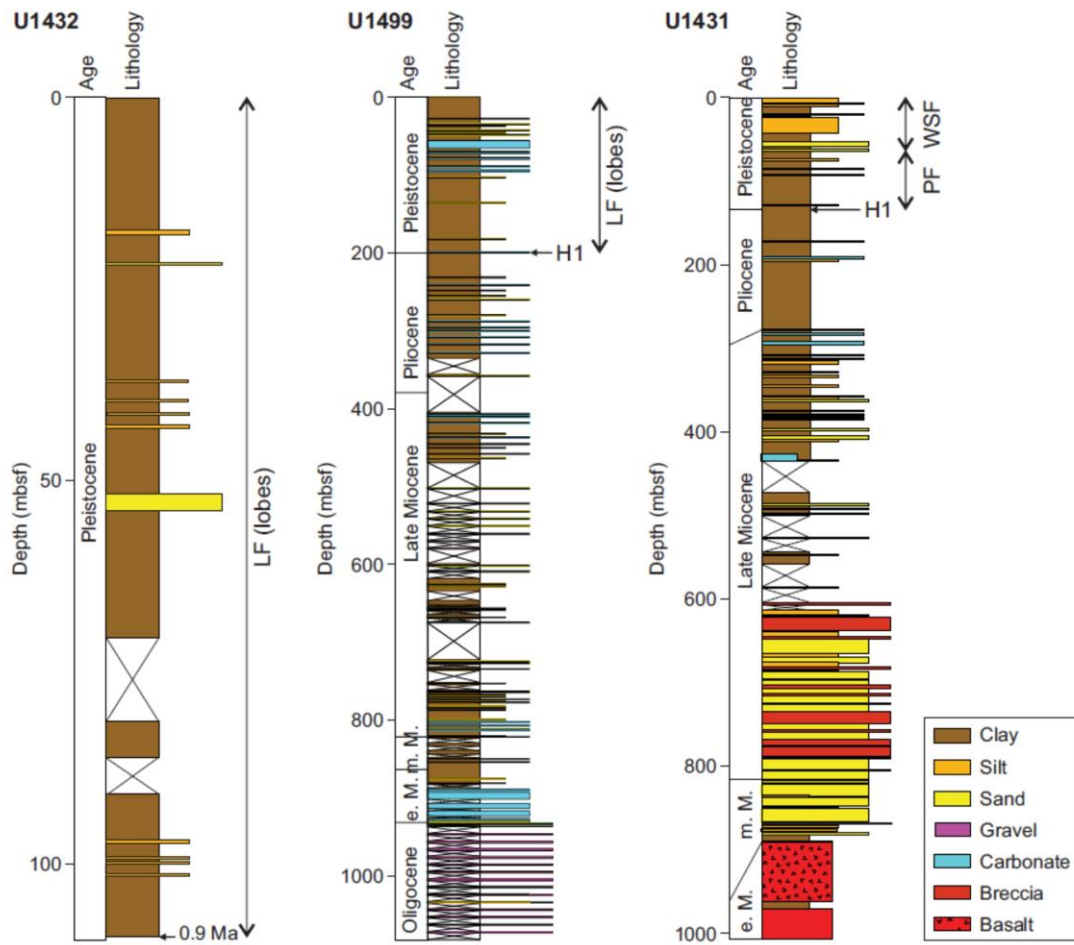
734

735

736   **Fig. 10**. Seismic profile across seamount S6. The dashed lines outline an area of

737   relatively high-amplitude seismic reflections on the north side of the seamount. PF =

738   parallel to subparallel seismic facies. Location of the seismic profile is shown in Fig.

739   2A.
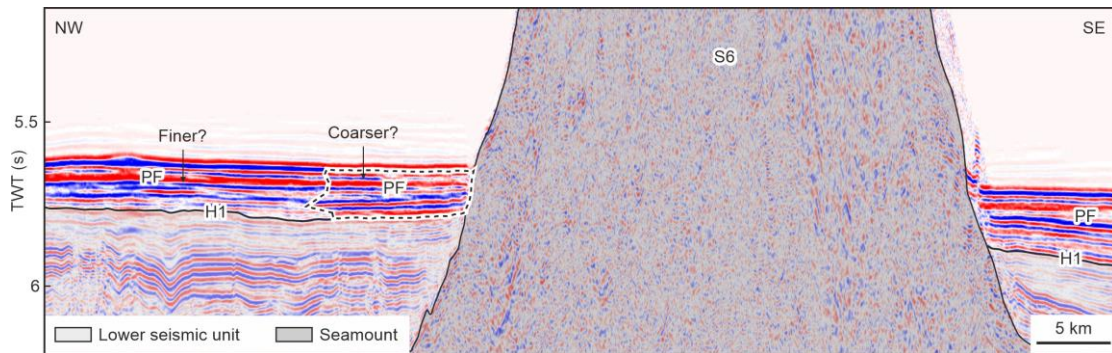
740

741

742 **Fig. 11**. Three-dimensional sketch of the depositional system of the northern South

743 China Sea abyssal plain. As turbidity currents flow across the flat open plain at the foot

744 of the continental margin and then into the rough terrain of seamounts and bedrock

745 ridges, the flow transitions from unconfined (depositional) to largely confined

746 (erosional). *PRMC* = Pearl River Mouth Canyon, FSR = fossil spreading ridge.
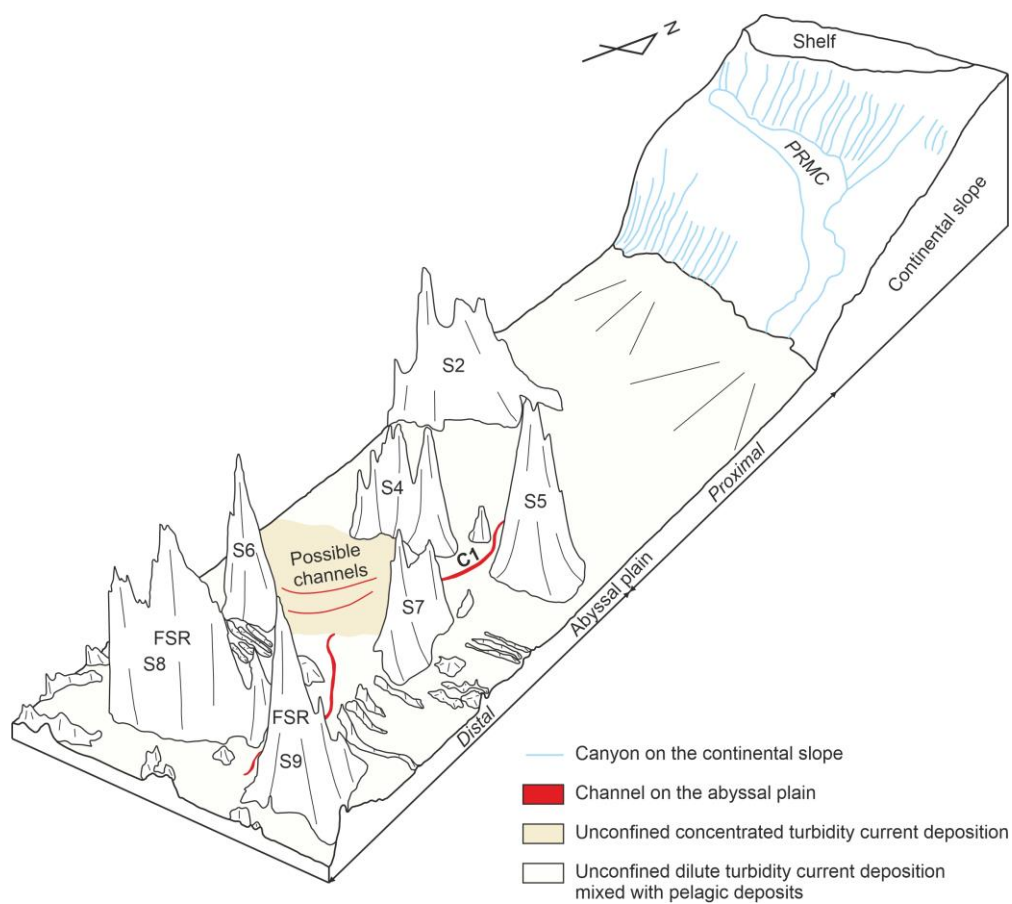
747
748

749   **References**

750

751   Alexander, J., Morris, S., 1994. Observations on experimental, nonchannelized, high-

752   concentration turbidity currents and variations in deposits around obstacles.

753   Journal of Sedimentary Research 64, 899–909.

754   Alfaro, E., Holz, M., 2014. Seismic geomorphological analysis of deepwater gravity-

755   driven deposits on a slope system of the southern Colombian Caribbean margin.

756   Marine and Petroleum Geology 57, 294–311.

757   Azpiro-zabala, M., Cartigny, M.J.B., Talling, P.J., Parsons, D.R., Sumner, E.J., Clare,

758   M.A., Simmons, S.M., Cooper, C.K., Pope, E.L., 2017. Newly recognized

759   turbidity current structure can explain prolonged flushing of submarine canyons.

760   Science advances 3(10), e1700200.

761   Bagnold, R. A., 1954. Experiments on a gravity-free dispersion of large solid spheres

762   in a Newtonian fluid under shear. Proceedings of the Royal Society of London.

763   Series A. Mathematical and Physical Sciences 225(1160), 49–63.

764   Beaubouef, R., Friedmann, S., 2000. High resolution seismic/sequence stratigraphic

765   framework for the evolution of Pleistocene intra slope basins, western Gulf of

766   Mexico: depositional models and reservoir analogs, Deep-water reservoirs of the

767   world: Gulf Coast Section SEPM 20th Annual Research Conference. SEPM, pp.

768   40–60.

769   Bellwald, B., Planke, S., Becker, L. W., Myklebust, R., 2020. Meltwater sediment

770   transport as the dominating process in mid-latitude trough mouth fan formation.

771   Nature communications 11(1), 1–10.

772   Bouma, A. H., Normark, W. R. & Barnes, N. E. 2012. Submarine Fans and Related

773   Turbidite Systems. Springer. Dordrecht.

774   Bouma, A. H., 2000. Coarse-grained and fine-grained turbidite systems as end member

775   models: applicability and dangers. Marine and Petroleum Geology 17(2), 137–

776   143.

777   Bouma, A.H., Stelting, C.E., Coleman, J.M., 1985. Mississippi fan, Gulf of Mexico. In:

778   Bouma, A.H., Normark, W.R., Barnes, N.E. (Eds.), Submarine Fans and Related

779   Turbidite Systems. Springer-Verlag, New York, pp. 143e150.

780   Bowen, A. J., Normark, W. R., & Piper, D. J. 1984. Modelling of turbidity currents on

781   Navy submarine fan, California continental borderland. Sedimentology, 31(2),

782   169–185.

783   Brooks, H. L., Hodgson, D. M., Brunt, R. L., Peakall, J., Hofstra, M., & Flint, S. S.,

784   2018. Deep-water channel-lobe transition zone dynamics: Processes and

785   depositional architecture, an example from the Karoo Basin, South Africa.

786   Bulletin, 130(9–10), 1723–1746.

787   Cartigny, M. J., Postma, G., van den Berg, J. H., & Mastbergen, D. R. 2011. A

788   comparative study of sediment waves and cyclic steps based on geometries,

789   internal structures and numerical modeling. Marine Geology, 280(1–4), 40–56.

790   Calder, B.R., Mayer, L.A., 2003. Automatic processing of high-rate, high-density

791   multibeam echosounder data. Geochemistry, Geophysics, Geosystems, 4 (6).

792   Catuneanu, O., Abreu, V., Bhattacharya, J., Blum, M., Dalrymple, R., Eriksson, P.,

793   Fielding, C.R., Fisher, W., Galloway, W., Gibling, M., 2009. Towards the

794   standardization of sequence stratigraphy. Earth Sci. Rev. 92, 1–33.

795   Daly, R.A., 1936. Origin of submarine canyons. American Journal of Science 5, 401–

796   420.

797   Damuth, J.E., Kumar, N., 1975. Amazon Cone: morphology, sediments, age, and

798   growth pattern. Geological Society of America Bulletin 86, 863–878.

799   de Leeuw, J., Eggenhuisen, J. T., & Cartigny, M. J. 2018. Linking submarine channel–

800   levee facies and architecture to flow structure of turbidity currents: insights from

801   flume tank experiments. Sedimentology, 65(3), 931–951.

802   Dennielou, B., Droz, L., Babonneau, N., Jacq, C., Bonnel, C., Picot, M., Saout, M.L.,

803   Saout, Y., Bez, M., Savoye, B., 2017. Morphology, structure, composition and

804   build-up processes of the active channel-mouth lobe complex of the Congo deep-

805   sea fan with inputs from remotely operated underwater vehicle (ROV) multibeam

806   and video surveys. Deep-sea Research Part Ii-topical Studies in Oceanography

807   142, 25–49.

808   Ding, W., Li, J., Han, X., Suess, E., Huang, Y., Qiu, X., Li, M., 2010. Morphotectonics

809   and formation of the Taiwan Bank Canyon, Southwest offshore Taiwan Island.

810   Journal of Oceanography and Marine Science 1, 65–78.

811   Ding, W., Li, J., Li, J., Fang, Y., Tang, Y., 2013. Morphotectonics and evolutionary

812   controls on the Pearl River Canyon system, South China Sea. Marine Geophysical

813   Research 34, 221–238.

814   Dixon, B.T., Weimer, P., 1998. Sequence stratigraphy and depositional history of the

815   eastern Mississippi Fan (Pleistocene), northeastern deep Gulf of Mexico. AAPG

816   bulletin 82, 1207–1232.

817   Droghei, R., Falcini, F., Casalbore, D., Martorelli, E., Mosetti, R., Sannino, G.,

818   Santoleri, R., Chiocci, F.L., 2016. The role of Internal Solitary Waves on deep-

819   water sedimentary processes: the case of up-slope migrating sediment waves off

820   the Messina Strait. Scientific reports 6.

821   Edwards, D., Leeder, M., Best, J.L., Pantin, H, 1994. On experimental reflected density

822   currents and the interpretation of certain turbidites. Sedimentology 41, 437–461.

823   Expedition 349 Scientists, 2014. South China Sea tectonics: Opening of the South

824   China Sea and its implications for Southeast Asian tectonics, climates, and deep

825   mantle processes since the late Mesozoic. International Ocean Discovery Program

826   Preliminary Report 349.

827   Expedition 367 Scientists, 2018. Expedition 367 Preliminary Report: South China Sea

828   Rifted Margin, 1–33.

829   Flood, R.D., Manley, P.L., Kowsmann, R.O., Appi, C.J., Pirmez, C., 1991. Seismic

830   facies and late Quaternary growth of Amazon submarine fan, Seismic facies and

831   sedimentary processes of submarine fans and turbidite systems. Springer, pp. 415–

832   433.

833 Flood, R.D., Shor, A.N., 1988. Mud waves in the Argentine Basin and their relationship

834   to regional bottom circulation patterns. Deep Sea Research Part A. Oceanographic

835   Research Papers 35, 943–971.

836 Galy V, France-Lanord C, Beyssac O, et al, 2007. Efficient organic carbon burial in the

837   Bengal fan sustained by the Himalayan erosional system. Nature 450(7168), 407–

838   410.

839 Gamberi, F., Rovere, M., Marani, M., 2011. Mass-transport complex evolution in a

840   tectonically active margin (Gioia Basin, Southeastern Tyrrhenian Sea). Marine

841   Geology 279, 98–110.

842 Gee, M. J. R., Gawthorpe, R. L., 2006. Submarine channels controlled by salt tectonics:

843   Examples from 3D seismic data offshore Angola. Marine and Petroleum Geology,

844   23, 443–458.

845 Gennaro, M., Wonham, J., Gawthorpe, R., Sælen, G., 2013. Seismic stratigraphy of the

846   Chalk Group in the Norwegian Central Graben, North Sea. Marine and Petroleum

847   Geology 45, 236–266.

848 Gong, C., Wang, Y., Zhu, W., Li, W., Xu, Q., Zhang, J., 2011. The Central Submarine

849   Canyon in the Qiongdongnan Basin, northwestern South China Sea: Architecture,

850   sequence stratigraphy, and depositional processes. Marine and Petroleum Geology

851   28, 1690–1702.

852 Hackbarth, C.J., Shew, R., 1994. Morphology and stratigraphy of a mid-Pleistocene

853   turbidite leveed channel from seismic, core and log data, northeastern Gulf of

854   Mexico, Submarine Fans and Turbidite Systems: SEPM, Gulf Coast Section, 15th

855   Annual Research Conference. SEPM, pp. 127–133.

856 Hage, S., Galy, V. V., Cartigny, M. J. B., Acikalin, S., Clare, M. A., Gröcke, D. R.,

857   Hilton, R. G., Hunt, J. E., Lintern, D. G., McGhee, C. A., Parons, D. R., Stacey,

858   C. D., Sumner, E. J., Talling, P. J., 2020. Efficient preservation of young terrestrial

859   organic carbon in sandy turbidity current deposits. Geology,

860   doi:10.1130/G47320.1,

861 Heerema, C. J., Talling, P. J., Cartigny, M. J., Paull, C. K., Bailey, L., Simmons, S. M.,

862   Anderson, K., 2020. What determines the downstream evolution of turbidity

863   currents? Earth and Planetary Science Letters 532, 116023.

864 Heezen, B. C., Ewing, W. M., 1952. Turbidity currents and submarine slumps, and the

865   1929 Grand Banks [Newfoundland] earthquake. American journal of Science

866   250(12), 849–873.

867 Heezen, B. C., Menzies, R. J., Schneider, R. J., Ewing, W. M., Granelli, N. C. L., 1964.

868   Congo submarine canyon. AAPG bulletin 48(7), 1126–1149.

869 Higuchi, Y., Yanagimoto, Y., Hoshi, K., Unou, S., Akiba, F., Tonoike, K., Koda, K.,

870   2007. Cenozoic stratigraphy and sedimentation history of the northern Philippine

871   Sea based on multichannel seismic reflection data. Island Arc 16, 374–393.

872 Hiscott, R., Pickering, K.J.N., 1984. Reflected turbidity currents on an Ordovician

873   basin floor, Canadian Appalachians 311, 143.

874 Hunt, J. E., 2017. Identifying and quantifying erosion beneath the deposits of long-

875   runout turbidity currents along their pathway. Marine Geology 389, 32–51.

876   Hunt, J. E., Wynn, R. B., Massin, D. G., Talling, P. J., Teagle, D. A. H., 2011.

877   Sedimentological and geochemical evidence for multistage failure of volcanic

878   island landslides: a case study from Icod landslide on north Tenerife, Canary

879   Islands. Geochemistry, Geophysics, Geosystems 12, 1–36.

880   Imran, J., Kassem, A., Khan, S. M. 2004. Three-dimensional modelling of density

881   current. I. Flow in straight confined and unconfined channels. Journal of Hydraulic

882   Research, 42(6), 578–590.

883   Jiang, T., Gao, H., He, J., Tian, D., 2019. Post-spreading volcanism in the central South

884   China Sea: insights from zircon U–Pb dating of volcaniclastic breccia and seismic

885   features. Marine Geophysical Research 40, 185–198.

886   Jobe, Z. R., Sylvester, Z., Parker, A. O., Howes, N., Slowey, N., Pirmez, C., 2015.

887   Rapid adjustment of submarine channel architecture to changes in sediment

888   supply. Journal of Sedimentary Research 85(6), 729–753.

889   Jobe, Z., Sylvester, Z., Pittaluga, M. B., Frascati, A., Pirmez, C., Minisini, D., ... &

890   Cantelli, A., 2017. Facies architecture of submarine channel deposits on the

891   western Niger Delta slope: Implications for grain-size and density stratification in

892   turbidity currents. Journal of Geophysical Research: Earth Surface, 122(2), 473–

893   491.

894   Judd, A.G., Hovland, M., 2007. Seabed Fluid Flow: The Impact on Geology, Biology

895   and the Marine Environment. Cambridge University Press, Cambridge, pp. 163–

896   178.

897   Kane, I.A., Clare, M.A., 2019. Dispersion, accumulation, and the ultimate fate of

898   microplastics in deep-marine environments: a review and future directions.

899   Frontiers in Earth Science 7, 1–27.

900   Karl, H., Cacchione, D., Carlson, P., 1986. Internal-wave currents as a mechanism to

901   account for large sand waves in Navarinsky Canyon head, Bering Sea. Journal of

902   Sedimentary Research 56, 706–714.

903   Komar, P. D. 1969. The channelized flow of turbidity currents with application to

904   Monterey deep-sea fan channel. Journal of Geophysical Research, 74(18), 4544–

905   4558.

906   Komar, P.D., 1973. Continuity of turbidity current flow and systematic variations in

907   deep-sea channel morphology. Geological Society of America Bulletin 84, 3329–

908   3338.

909   Kumar, A., Dutt, S., Saraswat, R., Gupta, A.K., Clift, P.D., Pandey, D.K., Yu, Z.,

910   Kulhanek, D.K., 2019. A late Pleistocene sedimentation in the Indus Fan, Arabian

911   Sea, IODP Site U1457. Geological Magazine, in press.

912   Li, C.F., Xu, X., Lin, J., Sun, Z., Zhu, J., Yao, Y., Zhao, X., Liu, Q., Kulhanek, D.K.,

913   Wang, J., 2014. Ages and magnetic structures of the South China Sea constrained

914   by deep tow magnetic surveys and IODP Expedition 349. Geochemistry,

915   Geophysics, Geosystems 15, 4958–4983.

916   Li, C. F. et al., 2015. Seismic stratigraphy of the central South China Sea basin and

917   implications for neotectonics. Journal of Geophysical Research: Solid Earth,

918   120(3), 1377–1399.

919   Liu, C.-S., Lundberg, N., Reed, D.L., Huang, Y.-L., 1993. Morphological and seismic

920   characteristics of the Kaoping Submarine Canyon. Marine Geology 111, 93–108.

921   McCave, I.N., 2017. Formation of sediment waves by turbidity currents and

922   geostrophic flows: A discussion. Marine Geology 390, 89–93.

923   Migeon, S., Savoye, B., Faugeres, J.C., 2000. Quaternary development of migrating

924   sediment waves in the Var deep-sea fan: distribution, growth pattern, and

925   implication for levee evolution. Sedimentary Geology 133, 265–293.

926   Middleton, G. V., Hampton, M. A. 1973. Part I. Sediment gravity flows: mechanics of

927   flow and deposition. In Turbidites and Deep Water Sedimentation, ed. G. V.

928   Middleton, A. H. Bouma, SEPM Pac. Sec. Short Course Notes. Anaheim, Calif:

929   SEPM. 38p.

930   Milliman, J. D., Syvitski, J. P., 1992. Geomorphic/tectonic control of sediment

931   discharge to the ocean: the importance of small mountainous rivers. The journal

932   of Geology 100(5), 525–544.

933   Mitchum, R.M., Vail Jr., P., Sangree, J.B., 1977. Seismic stratigraphy and global

934   changes of sea level, Part 6: Stratigraphic interpretation of seismic reflection

935   patterns in depositional sequences. In: Payton, C.E. (Ed.), Seismic Stratigraphy—

936   Applications to Hydrocarbon Exploration. The American Association of

937   Petroleum Geologists, Tulsa, pp. 117–134.

938   Moscardelli, L., Wood, L., 2008. New classification system for mass transport

939   complexes in offshore Trinidad. Basin Research 20, 73–98.

940 Mutti, E., Normark, W.R., 1987. Comparing examples of modern and ancient turbidite

941 systems: problems and concepts, in: Legget, J.K., Zuffa, G.G. (Eds.), Marine

942 Clastic Sedimentology. Graham and Trotman, London, pp. 1–38.

943 Mutti, E., 1992. Turbidite sandstones. Agip, San Donato Milanese.

944 Normark, W.R., Hess, G.R., Stow, D.A.V., Bowen, A.J., 1980. Sediment waves on the

945 monterey fan levee: A preliminary physical interpretation. Marine Geology 37, 1–

946 18.

947 Normark, W. R., 1970. Growth patterns of deep-sea fans. AAPG bulletin 54(11), 2170–

948 2195.

949 Palanques, A., Kenyon, N. H., Alonso, B., & Limonov, A., 1996. Erosional and

950 depositional patterns in the Valencia Channel mouth: an example of a modern

951 channel-lobe transition zone. Marine Geophysical Researches 18(1), 104–118.

952 Parsons, J. D., Schweller, W. J., Stelting, C. W., Southard, J. B., Lyons, W. J.,

953 Grotzinger, J. P., 2002. A preliminary experimental study of turbidite fan deposits.

954 Journal of Sedimentary Research 72(5), 619–628.

955 Pearce, T. J., Jarvis, I., 1992. Composition and provenance of turbidite sands: late

956 Quaternary, Maderia Abyssal Plain. Marine Geology 109, 21–51.

957 Pickering, K.T., Underwood, M.B., Saito, S., Naruse, H., Kutterolf, S., Scudder, R.P.,

958 Park, J., Moore, G.F., Slagle, A.L., 2013. Depositional architecture, provenance,

959 and tectonic/eustatic modulation of Miocene submarine fans in the Shikoku Basin:

960 Results from Nankai Trough Seismogenic Zone Experiment. Geochemistry

961 Geophysics Geosystems 14, 1722–1739.

962 Piper, D.J., Normark, W.R., 1983. Turbidite depositional patterns and flow

963   characteristics, Navy submarine fan, California Borderland. Sedimentology 30,

964   681–694.

965 Piper, D.J.W., Normark, W.R., 2009. Processes that initiate turbidity currents and their

966   influence on turbidites: A marine geology perspective. Journal of Sedimentary

967   Research 79, 347–362.

968 Pirmez, C., Imran, J., 2003. Reconstruction of turbidity currents in Amazon Channel.

969   Marine and Petroleum Geology 20, 823–849.

970 Pohl, F. (2019). Turbidity currents and their deposits in abrupt morphological transition

971   zones (Doctoral dissertation, Utrecht University).

972 Pohl, F., Eggenhuisen, J.T., Tilston, M., Cartigny, M.J.B., 2019. New flow relaxation

973   mechanism explains scour fields at the end of submarine channels. Nature

974   communications 10, 4425.

975 Pohl, F., Eggenhuisen, J. T., Kane, I. A., Clare, M. A. 2020. Transport and burial of

976   microplastics in deep-marine sediments by turbidity currents. Environmental

977   Science and Technology 54(7), 4180–4189.

978 Posamentier, H.W., Walker, R.G., 2006. Facies models revisited. SEPM. Tulsa.

979 Prather, B.E., Booth, J.R., Steffens, G.S., Craig, P.A., 1998. Classification, lithologic

980   calibration, and stratigraphic succession of seismic facies of intraslope basins,

981   deep-water Gulf of Mexico. AAPG bulletin 82, 701–728.

982 Prather, B.E., 2003. Controls on reservoir distribution, architecture and stratigraphic

983   trapping in slope settings. Marine and Petroleum Geology, 20(6–8), 529–545.

984 Prather, B. E., et al., 2012. Stratigraphic response to evolving geomorphology in a

985   submarine apron perched on the upper Niger Delta slope. Society for Sedimentary

986   Geology (SEPM) Special Publication 99, 145–161.

987 Pratson, L.F., Ryan, W.B.F., Mountain, G.S., Twichell, D.C., 1994. Submarine canyon

988   initiation by downslope-eroding sediment flows: Evidence in late Cenozoic strata

989   on the New Jersey continental slope. Geological Society of America Bulletin 106,

990   395–412.

991 Puig, P., Palanques, A., Martín, J., 2014. Contemporary sediment-transport processes

992   in submarine canyons. Annual review of marine science 6, 53–77.

993 Rabouille, C. et al., 2017. The Congolobe project, a multidisciplinary study of Congo

994   deep-sea fan lobe complex: Overview of methods, strategies, observations and

995   sampling. Deep Sea Research Part II: Topical Studies in Oceanography 142, 7–

996   24.

997 Reeder, D.B., Ma, B.B., Yang, Y.J., 2011. Very large subaqueous sand dunes on the

998   upper continental slope in the South China Sea generated by episodic, shoaling

999   deep-water internal solitary waves. Marine Geology 279, 12–18.

1000 Ribó, M., Puig, P., Urgeles, R., Van Rooij, D., Muñoz, A., 2016. Spatio-temporal

1001   evolution of sediment waves developed on the Gulf of Valencia margin (NW

1002   Mediterranean) during the Plio-Quaternary. Marine Geology 378, 276–291.

1003 Richards, M., Bowman, M., Reading, H., 1998. Submarine-fan systems i:

1004   characterization and stratigraphic prediction. Marine and Petroleum Geology 15,

1005   689–717.

1006   Rimington, N., Cramp, A., Morton, A., 2000. Amazon Fan sands: implications for

1007   provenance. Marine and Petroleum Geology 17(2), 267–284.

1008   Rothwell, R.G., Alibes, B., Weaver, P.P.E., 1998. Seismic facies of the Madeira

1009   Abyssal Plain: A correlation between seismic reflection profile and borehole data.

1010   Proceedings of the Ocean Drilling Program Scientific Results 157, 473–498.

1011   Saller, A.H., Noah, J.T., Ruzuar, A.P., Schneider, R., 2004. Linked lowstand delta to

1012   basin-floor fan deposition, offshore Indonesia: An analog for deep-water reservoir

1013   systems. AAPG bulletin 88, 21–46.

1014   Sangree, J., Widmier, J., 1977. Seismic stratigraphy and global changes of sea level,

1015   part 9: seismic interpretation of clastic depositional facies. AAPG bulletin 62,

1016   752–771.

1017   Savoye, B., Babonneau, N., Dennielou, B., Bez, M., 2009. Geological overview of the

1018   Angola–Congo margin, the Congo deep-sea fan and its submarine valleys. Deep

1019   Sea Research Part II: Topical Studies in Oceanography 56, 2169–2182.

1020   Schwenk, T., 2004. The Bengal Fan: architecture, morphology and depositional

1021   processes at different scales revealed from high-resolution seismic and

1022   hydroacoustic data. Ph.D. Thesis, Univercity Bremen. Bremen, Germany.

1023   Sibuet, J.-C., Yeh, Y.-C., Lee, C.-S., 2016. Geodynamics of the South China Sea.

1024   Tectonophysics 692, 98–119.

1025   Slootman, A., Cartigny, M. J., 2020. Cyclic steps: review and aggradation-based

1026   classification. Earth-Science Reviews 201, 102949.

1027   Stevenson, C. J., Talling, P. J., Wynn, R. B., Masson, D. G., Hunt, J. E., Frenz, M.,

1028   Akhmetzhanhov, A., Cronin, B. T. 2013. The flows that left no trace: Very large-

1029   volume turbidity currents that bypassed sedimen through submarine channels

1030   without eroding the seafloor. Marine and Petroleum Geology 41, 186–205.

1031   Stevenson, C.J., Jackson, C.A.-L., Hodgson, D.M., Hubbard, S.M., Eggenhuisen, J.T.,

1032   2015. Deep-water sediment bypass. Journal of Sedimentary Research 85(9),

1033   1058–1081.

1034   Su, J., Zhong, G., 2020. Sedimentary and petrophysical characteristics of various

1035   turbidites at IODP Sites U1499 and U1500 in the northern South China Sea.

1036   MARINE GEOLOGY & QUATERNARY GEOLOGY 40 (3), 13–24 (in Chinese

1037   with English abstract).

1038   Su, M., Xie, X., Xie, Y., Wang, Z., Zhang, C., Jiang, T., He, Y., 2014. The

1039   segmentations and the significances of the Central Canyon System in the

1040   Qiongdongnan Basin, northern South China Sea. Journal of Asian Earth Sciences

1041   79, 552–563.

1042   Sun, Q., Wu, S., Cartwright, J., Dong, D., 2012. Shallow gas and focused fluid flow

1043   systems in the Pearl River Mouth Basin, northern South China Sea. Marine

1044   Geology 315, 1–14.

1045   Sun, Q., Xie, X, Piper, D. J., Wu, J., Wu, S., 2017. Three dimensional seismic anatomy

1046   of multi-stage mass transport deposits in the Pearl River Mouth Basin, northern

1047   South China Sea: Their ages and kinematics. Marine Geology 393, 93–108.

1048 Symons, W. O., Sumner, E. J., Talling, P. J., Cartigny, M. J., Clare, M. A., 2016. Large-

1049   scale sediment waves and scours on the modern seafloor and their implications for

1050   the prevalence of supercritical flows. Marine Geology 371, 130–148.

1051 Talling, P.J., 2014. On the triggers, resulting flow types and frequencies of subaqueous

1052   sediment density flows in different settings. Marine Geology 352, 155–182.

1053 Talling, P. J., et al., 2015. Key Future Directions For Research On Turbidity Currents

1054   And Their Depositskey Future Directions For Research On Turbidity Currents

1055   And Their Deposits. Journal of Sedimentary Research 85(2), 153–169.

1056 Taylor, B., Hayes, D.E., 1980. The tectonic evolution of the South China Basin.

1057   Geophysical Monograph Series 23, 89–104.

1058 Tinterri, R., Civa, A., Laporta, M., Piazza, A., 2020. Turbidites and turbidity currents,

1059   in Scarselli, N., Adam, J., Chiarella, D., Roberts, D., Bally, A. (Eds.), Regional

1060   Geology and Tectonics. Volume 1: Principles of Geologic Analysis. Elsevier,

1061   Oxford, pp. 441–479.Waltham, D. 2004. Flow transformations in particulate

1062   gravity currents. Journal of Sedimentary Research, 74(1), 129–134.

1063 Wang, D., Wu, S., Qin, Z., Spence, G., Lu, F., 2013. Seismic characteristics of the

1064   Huang mass transport deposits in teh Qiongdongnan Basin, South China Sea:

1065   Implications for regional tectonic activity. Marine Geology 346, 165–182.

1066 Wang, L., Wang, Z., Yu, S., Ngia, N.R., 2016. Seismic responses and controlling

1067   factors of Miocene deepwater gravity-flow deposits in Block A, Lower Congo

1068   Basin. Journal of African Earth Sciences 120, 31–43.

1069   Wang X, Wu M, 1984. Some geochemical cgaracteristics of basalts in the South China

1070   Sea. Geochemica 4, 332–339 (in Chinese with English abstract).

1071   Wells, M. G., Dorrell, R. M., 2021. Turbulence processes within turbidity currents.

1072   Annual Review of Fluid Mechanics 53, 59–83.

1073   Wynn, R.B., Cronin, B.T., Peakall, J., 2007. Sinuous deep-water channels: Genesis,

1074   geometry and architecture. Marine and Petroleum Geology 24, 341–387.

1075   Wynn, R.B., Stow, D.A.V., 2002. Classification and characterisation of deep-water

1076   sediment waves. Marine Geology 192, 7–22.

1077   Wynn, R. B., Weaver, P. P., Masson, D. G., Stow, D. A., 2002. Turbidite depositional

1078   architecture across three interconnected deep-water basins on the north-west

1079   African margin. Sedimentology 49(4), 669–695.

1080   Xia, S., Zhao, F., Zhao, D., Fan, C., Wu, S., Mi, L., Sun, J., Cao, J., Wan, K., 2018.

1081   Crustal plumbing system of post-rift magmatism in the northern margin of South

1082   China Sea: New insights from integrated seismology. Tectonophysics 744, 227–

1083   238.

1084   Yan, Q., Shi, X., Wang, K., Bu, W., Xiao, L., 2008. Major element, trace element, and

1085   Sr, Nd and Pb isotope studies of Cenozoic basalts from the South China Sea.

1086   Science in China Series D: Earth Sciences 51, 550–566.

1087   Yang, S., Qiu, Y., Zhu, B., Chen, J., Guan, Y., Peng, X., 2015. Atlas of geology and

1088   geophysics of the South China Sea. China Navigation Publications, Tianjin

1089　Yin, S., Lin, L., Pope, E.L., Li, J., Ding, W., Wu, Z., Ding, W., Gao, J., Zhao, D., 2019.

1090　　　Continental slope-confined canyons in the Pearl River Mouth Basin in the South

1091　　　China Sea dominated by erosion, 2004–2018. Geomorphology 344, 60–74.

1092　Yin, S., Li, J., Ding, W., Sawyer, D. E., Wu, Z., Tang, Y. 2020. Sedimentary filling

1093　　　characteristics of the South China Sea oceanic basin, with links to tectonic activity

1094　　　during and after seafloor spreading. International Geology Review, 62(7–8), 887–

1095　　　907.

1096　Yin, S., Wang, L., Guo, Y., Zhong, G., 2015. Morphology, sedimentary characteristics,

1097　　　and origin of the Dongsha submarine canyon in the northeastern continental slope

1098　　　of the South China Sea. Science China Earth Sciences 58, 971–985.

1099　Yu, H.S., Chang, J.F., 2002. The Penghu submarine canyon off southwestern Taiwan:

1100　　　morphology and origin. Terrestrial Atmospheric and Oceanic Sciences 13, 547–

1101　　　562.

1102　Zhu, M., Graham, S., Pang, X., McHargue, T., 2010. Characteristics of migrating

1103　　　submarine canyons from the middle Miocene to present: Implications for

1104　　　paleoceanographic circulation, northern South China Sea. Marine and Petroleum

1105　　　Geology 27, 307–319.

1106